

ABSTRACT

Title of thesis: SCALABLE, COMPOSABLE OPERATORS
FOR DEFECT DESIGN AND ANALYSIS

Rose Weisburgh, Master of Science, 2016

Thesis directed by: Professor Peter W Chung
Department of Mechanical Engineering

It is well understood that defects adversely affect the electro-mechanical properties of materials. Ideally, defect compositions of raw materials used in devices could be measured, but present technology in the field of atomic defect detection is either destructive in nature, or is unable to determine the precise atomic composition of materials. In the adjacent field of damage detection in large-scale truss networks, algorithms based on spectral measurements have successfully been employed to locate damaged members. Already similar principles have been applied to material lattices experimentally by using Raman Spectroscopy to qualitatively approximate defect densities within materials. However, the applications have largely been limited to surface defects or two-dimensional materials, and the host lattices and defect types are primarily studied anecdotally.

This thesis details a numerical method for determining the precise phonon or vibration spectra of material lattices with defects, as it was originally presented in [1]. The dynamical matrices of lattices containing defects are calculated by introducing defects systematically into the dynamical matrices of pristine, defect-free

lattices using linear operators. Each operation modifies or removes an individual bond or interaction. Complex defect configurations can be composed through re-iterative application of the operators. The proposed methods may be applied to systems containing any interaction type or bond order, including space trusses and atomic lattices. The method is demonstrated by numerically determining the convergence rate of phonon properties in the dilute limit of a single point vacancy. Then the same methodology is applied to two-dimensional atomic lattices with central forces, two-dimension truss networks with distributed mass, as well as three-dimensional atomic lattices with non-linear many body potentials. In each example, the defect structure and properties are shown to alter the spectral properties of the materials.

SCALABLE, COMPOSABLE OPERATORS
FOR DEFECT DESIGN AND ANALYSIS

by

Rose Weisburgh

Thesis submitted to the Faculty of the Graduate School of the
University of Maryland, College Park in partial fulfillment
of the requirements for the degree of
Master of Science
2016

Advisory Committee:
Professor Peter W Chung, Chair/Advisor
Professor Abhijit Dasgupta
Professor Miao Yu

© Copyright by
Rose Weisburgh
2016

Acknowledgments

I would first like to thank my research advisor, Professor Peter W. Chung. Throughout this process, he has always made time to discuss my research progress, and provide guidance on potential next steps. Furthermore, he has always listened to and respected my opinions and points of view. I know that I would not have completed the work in this thesis without his guidance and support, nor would I have received a fellowship for future work without his recommendation and foresight.

I would also like to thank Dr. Madan Dubey in the RF-Division of the Sensors and Electron Devices Directorate at the Army Research Lab, and the nanoelectronics team for exposing me to some practical applications of this research during my summer with the Army Research Lab. Additionally, thanks to Dr. Raju R. Namburu in the Computational Sciences Division of the Computational and Information Science Directorate, the Army Research Office, and the Oak Ridge Institute for Science and Education for supporting this research, and providing a hands-on opportunity for me to learn experimental techniques and tools. I would also like to thank the Army Research Office's Mathematical Science Division, the Center for Engineering Concepts Development, and the Department of Mechanical Engineering at the University of Maryland who supported portions of this work.

Finally, I would like to express my sincere gratitude towards my parents, Mitch and Karin, and my partner, Dan, for their continued support and understanding. Thank you.

Table of Contents

| | |
|--|----|
| List of Figures | v |
| 1 Introduction | 1 |
| 1.1 Literature Review | 6 |
| 1.1.1 Atomic Defect Dynamics | 7 |
| 1.1.2 Microstructure and Continuum Analyses | 10 |
| 1.1.3 Structural Health Monitoring in Truss Networks | 12 |
| 2 Methodology | 15 |
| 2.1 Overview | 15 |
| 2.2 Defect Operator Derivation | 22 |
| 2.2.1 Additive Potential Energy | 22 |
| 2.2.2 Central Forces | 25 |
| 2.2.2.1 Lattice Dynamical Equations | 25 |
| 2.2.2.2 Defect Operators for Central Forces | 31 |
| 2.2.3 Embedded Atom Method | 34 |
| 2.2.3.1 Lattice Dynamics for EAM potentials | 38 |
| 2.2.3.2 Defect Operators for EAM Potential | 41 |
| 3 Results and Analysis | 44 |
| 3.1 Convergence to the Dilute Defect Limit in a 1D Lattice Chain | 44 |
| 3.2 2D Rectangular Lattices with Central Forces | 52 |
| 3.2.1 Example Set-up | 53 |
| 3.2.2 Point Defect in Square Lattice | 58 |
| 3.2.3 Defect in Space Truss | 67 |
| 3.3 Emulating Relaxation in a HCP Lattice with EAM Potential | 78 |
| 3.3.1 Relaxation in Magnesium | 79 |
| 3.3.2 Use of the Operator Method to Simulate Relaxation | 83 |
| 4 Conclusion | 90 |
| 4.1 Contributions | 90 |
| 4.2 Future Work | 92 |

| | |
|----------------------------|-----|
| A Orthogonality Conditions | 95 |
| Bibliography | 100 |

List of Figures

| | | |
|------|---|----|
| 1.1 | Defective Raman spectrum | 2 |
| 1.2 | Schematic of potential defect-induced changes to the vibration spectrum | 3 |
| | | |
| 2.1 | Vacancy schematic | 17 |
| 2.2 | Periodic lattice schematic | 26 |
| 2.3 | EAM potential energy functions | 37 |
| 2.4 | Dispersion curves of Mg using an EAM potential | 42 |
| | | |
| 3.1 | Defect in the unit cell of a one dimensional chain | 44 |
| 3.2 | Dispersion curves for 1D pristine lattice | 47 |
| 3.3 | Dispersion curves for 1D defective lattice | 48 |
| 3.4 | Frequency shift due to defective mass in a 1D lattice | 50 |
| 3.5 | Frequency shift due to bond potential in a 1D lattice | 50 |
| 3.6 | Convergence to the dilute limit | 51 |
| 3.7 | Defect geometries in a 2D square lattice | 54 |
| 3.8 | Brillouin zone of rectangular lattice | 60 |
| 3.9 | Density of states of a point defect in a square lattice | 61 |
| 3.10 | Phonon spectrum of a pristine square lattice | 61 |
| 3.11 | Phonon spectrum of a point defect in a square lattice | 62 |
| 3.12 | Modal shifts due to point defect | 64 |
| 3.13 | TA mode shapes in a square lattice | 66 |
| 3.14 | Phonon spectrum of a defective truss in a square lattice | 71 |
| 3.15 | Phonon spectrum of a defective truss in a square lattice | 72 |
| 3.16 | Modal shifts due to a defective truss | 74 |
| 3.17 | Mode shapes of high energy TA mode | 75 |
| 3.18 | Mode shapes of low energy TA mode | 76 |
| 3.19 | Magnesium unit cell with vacancy | 80 |
| 3.20 | Relaxed and unrelaxed spectra of magnesium | 82 |
| 3.21 | Relaxation parameters for magnesium vacancy in 2^3 lattice | 85 |
| 3.22 | Detailed error plots for a vacancy in 2^3 lattice with $\mu = 0.05$ | 86 |
| | | |
| A.1 | Primitive cells for basic lattice geometries | 96 |

Chapter 1: Introduction

Defects or disorder in material lattices at the atomic or continuum scale can significantly alter material properties. In atomic lattices, defects have been known to affect the failure response, electronic band structure, carrier transport, and phase transitions of materials. In the semiconductor industry, where devices are now designed on the nano scale, each atomic defect has a larger effect on the overall device properties than ever before. Thus it is becoming increasingly important to know the atomic composition of the device materials through non-destructive measurements. Furthermore, a fundamental understanding of the effects of defects on material properties could enable the design of superior materials and devices.

Techniques exist for visually observing defects using tools such as transmission electron microscopy [3]. However, visual tools cannot provide detailed information about defects within the bulk of the material nor are they able to predict the effect of defects on material properties. Concomitantly, spectral techniques such as Raman spectroscopy, have been used to qualitatively detect defect densities through variations in the vibration spectra of well-studied materials [2,4-6]. As an example, Fig. 1.1 (originally from [2]) displays the Raman spectrum of graphene with different concentrations of hydrogen atoms. Each peak on the plot may be interpreted

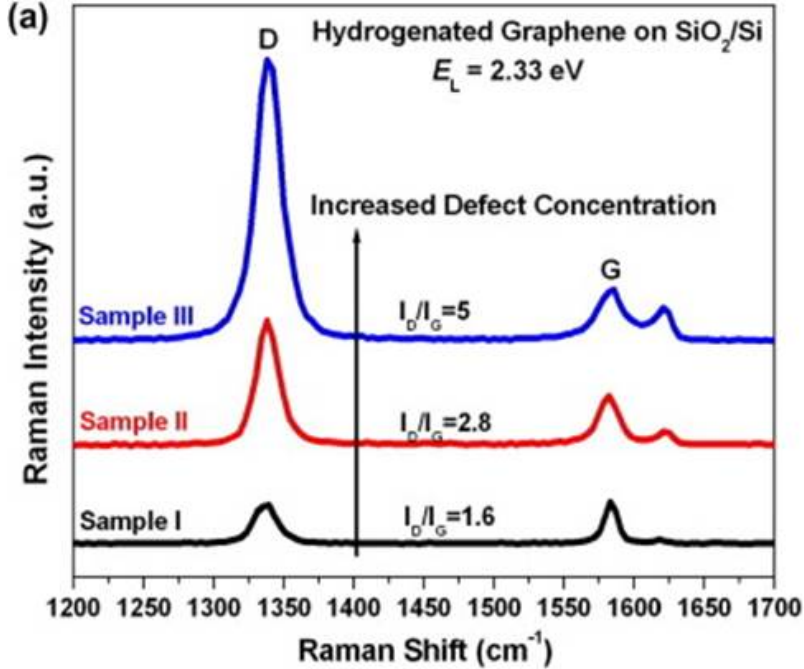


Figure 1.1: The effects of defect density on the Raman spectrum of hydrogenated graphene, as expressed in [2]. As shown, increasing the defect density directly results in an increase of the relative amplitude (I_D/I_G) of the peak labeled as ‘D’ as compared to the peak labeled as ‘G’.

as a resonant frequency of the material. Luo et. al. [2] note two key observations from Fig. 1.1. First, the relative amplitude of the two resonant frequencies labeled as ‘D’ and ‘G’ change as the defect concentration varies. The amplitude of ‘D’ changes from a factor of 1.6 to a factor of 5 times larger than the amplitude of the ‘G’ peak. Secondly, the ‘G’ peak splits into two distinct peaks at high defect densities. Noting these observations, one could conceivably perform a spectroscopic measurement on a sample of graphene and approximate the concentration of hydrogen atoms from the number of unique peaks and relative intensity between peaks. Spectral techniques for detecting defects, like the Raman measurements in Fig. 1.1, are a natural choice for defect detection because they are non-destructive, and also because electro-mechanical properties of materials are directly calculable from vibra-

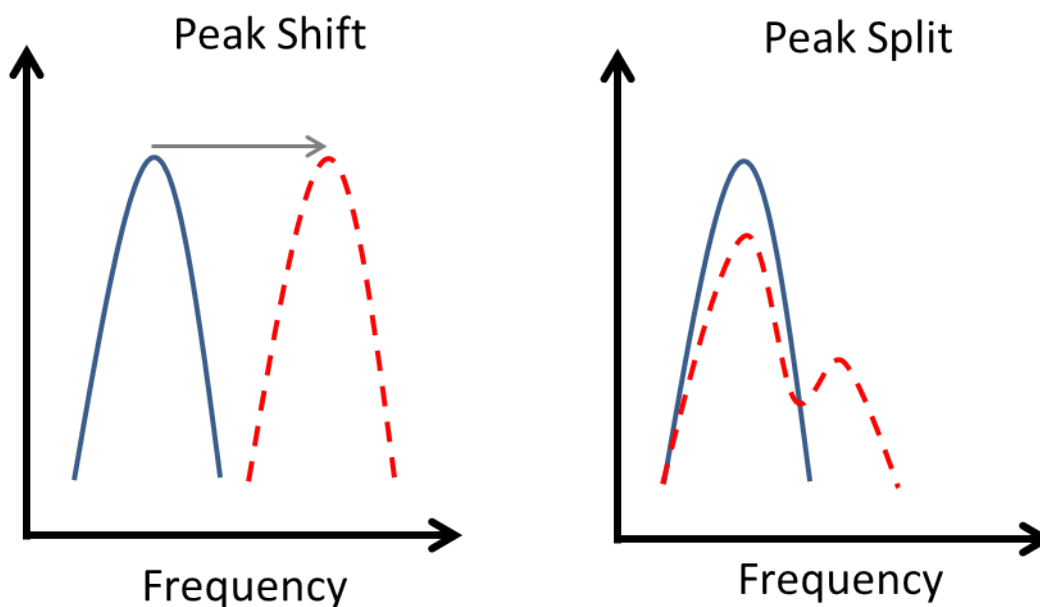


Figure 1.2: Two possible effects of defects on the vibration spectrum are shown. On the left, the peak frequency of vibration shifts to a higher frequency value. On the right, a single peak in the frequency spectrum splits into two distinct peaks.

tion spectra. Therefore the quantification of the effect of defects on vibration spectra could not only enable defect detection, but also provide insight to the properties of defective materials.

Two effects that defects may have on the spectral properties of a material are shifts and splits of the peak frequencies in the vibration spectrum, schematically depicted in Fig. 1.2. Defect-induced spectral shifts and splits are highly dependent on both the host lattice and the defect properties. Atomic-scale defect dynamics has been a widely studied area to predict the effect of defects on the vibration or phonon spectra of materials for applications in non-destructive defect detection as well as defect or dopant design. Theoretical calculations [7–9], physical experiments [2,4,6], and numerical experiments [10], such as molecular dynamics simulations, have all

been employed to study defect induced changes of phonon frequencies. The input to any of these methodologies is a fixed system, either virtual or physical, with certain lattice and defect structures, and specific defect parameters (such as mass or charge of an interstitial atom). Thus precise knowledge of the atomic configuration of the defect is a prerequisite for accurate calculation of both lattice and electronic properties. Since each unique individual defect, combination of defects, and relative orientation between defects gives rise to unique system properties, it is necessary to perform calculations, measurements, or simulations anew for each defective lattice of interest. Therefore, while it is a straightforward matter of calculating the phonon spectrum given the nodal interactions or bonds in a lattice, there is a dearth of analytical tools to examine structure-property relationships when defects are present. As a result, even in simulation, the effects of defects in material lattices are largely studied anecdotally.

At the continuum scale, the ability to alter the phonon spectra of materials has wide-reaching applications including vibration and noise control through acoustic filters [11]. Defect engineering [12] is one method of altering the phonon spectra of materials, breaking system symmetries, and inducing shifts of phonon frequencies and splits of certain degenerate solutions. However, like atomic-level methodologies, the current defect analysis techniques independently analyze each individual defect design of interest. Thus defect design is difficult since no clear relationship exists between defect parameters – e.g. mass, potential, density, geometry – and spectral shifts.

Conversely, a rich history exists for quantifying degrees of damage using the

vibration spectra of large-scale truss networks [13]. The dynamic equations for modeling material lattices are not, in principle, different from the equations used to model large-scale truss networks [14]. The primary differences arise from the nonlinear potential energy functions and the presence of many-body interactions in atomic lattices. In many cases, including [7–9], the interatomic potential between atoms is assumed to be linear, or harmonic, and the types of interactions investigated are limited to pair potentials. Under these specific assumptions, a material lattice is nothing more than a truss network with a high connectivity between nodes, and the calculation of the material phonon spectrum is no different from the calculation of the natural frequencies of a truss structure. It follows that the vast techniques developed for predicting the vibration spectra of defective truss networks may be applied to the computation of phonon spectra of defective material lattices, at least under the harmonic approximation and in the absence of relaxation.

In spite of the infinite number of possible defect configurations, in this thesis I derive a new methodology for atomic and continuum-scaled lattice dynamics inspired by the “Model Updating Methods” described in [13] and the heuristic model proposed by Kabe in [15] for truss networks. The methodology derivation makes no assumptions about bond order, scale, or mass distribution, and is not only applicable to atomic lattices, but may also be applied to structural truss networks and continuum-level material models. As such, the terminology used presently is nodes and interactions, where a node may be an atom or a joint, and an interaction may be a bond, material element, or truss. The premise behind the derivation is that a pristine or perfect system may be described through the combination of a dynamical

matrix or stiffness matrix \mathbf{D}_p , which captures the geometry and material properties of the interactions in the pristine lattice, and a mass matrix \mathbf{M}_p , which contains the inertial properties of the pristine lattice. In Section 2 linear operators are derived to manipulate these two pristine matrices into defective states. The operators, in turn, may be used to reiteratively build compound defects composed of multiple damaged, modified, or missing interactions. Furthermore, defect parameters can be introduced and varied within the operator to analyze the effects of defect mass or changes to the interaction strength as in the case of substitutional defects. Thus the pristine matrices need only be computed a single time, but infinitely many defective spectra may be calculated through the application of individual defect operators, or combinations of multiple defect operators. In a manner of speaking, this also incidentally enables a computable framework for the Lifshitz formalism [16] and the theory of [7] that avoids the use of Green’s functions. Furthermore, the resulting defective frequencies using the operator method are exact under the harmonic approximation.

1.1 Literature Review

This work relates to and draws from the fields of defect dynamics in atomic lattices, phononic or granular media at the continuum-scale, and damage in large-scale truss networks. The methodology proposed herein may be applied to defective or damaged systems across all length scales: atomic, micro-structure, continuum, or structural. The literature review is presented in three sections. Section 1.1.1

discusses the original defect dynamic techniques [7,9] and later expansions on these theories, along with numerical and physical experimental works related to the spectral properties of defective materials. Extensions of the lattice dynamic and defect dynamic principles to micro-structure and continuum-level systems are reviewed in Section 1.1.2. Finally, operator-based methodologies for locating damage in truss-networks are discussed in Section 1.1.3.

1.1.1 Atomic Defect Dynamics

In this work a “defect” is defined as an alteration of mass or interatomic potential in an otherwise uniform lattice. In a broad sense, dopants or even alloys may be interpreted as defects in the absence of phase changes, and a dopant concentration or alloy material percentage are both synonymous with defect density. This work therefore relates to, and draws from not only the fields of defect dynamics in crystalline materials, but also to the varied works related to the spectroscopy of materials with altered atomic compositions. Theoretical calculations, spectroscopic measurements, and molecular dynamic simulations have all been used to determine the effect of defects on material properties. The works described herein outline just a few of the many studies relating material composition at the atomic level to measured or calculated spectroscopic properties.

In the field of defect dynamics, Green’s Function-based methodologies have been used to calculate changes in lattice spectra due to defects. Montroll and Potts developed theory to calculate the localized changes in frequency due to point

defects [7]. Recognizing the $r^{-1} \exp(-Ar)$ decay of the effect of point defects at large distances, they developed a Green's function-based technique to study single defects and defect pairs in one-dimensional chains with extended arguments for three-dimensional lattices. In their most simplistic example, a single point defect in an infinite chain, Montroll and Potts were able to compute an analytical formula relating the mass and interatomic potential of a single point defect to the frequency shift of the highest phonon mode. However, no similar relations were presented between defect properties and phonon modes for systems with added complexity, such as multiple dimensions. Lifshitz and Kosevich [9] developed a more expansive approach to defect dynamics. They were able to calculate changes to the local and bulk spectra of materials due to point, line, and planar defects. Each of these articles helped to create a rigorous, physical understanding of the modal properties of defective lattices. However, both rely on Green's functions which make extensions to complex lattice structures a challenge.

Recently, Grimm and Wagner [17] expanded the Lifshitz formalism of [16], to calculate the effect of densely populated one-dimensional defects on the thermodynamic properties of three-dimensional crystalline materials. Grimm and Wagner's methods increased the efficiency of the Lifshitz formulae by defining 'mesoscopic' coordinates, effectively reducing the rank of the tensors. The proposed method increased the breadth and computability of the Lifshitz formalism, but continued to utilize Green's functions for calculations, and the examples in [17] were limited to simple cubic lattices with nearest-neighbor interactions to enable the use of exact, analytical functions. The method enabled the investigation of defect mechanisms in

crystals that could mimic low temperature behavior of glassy materials.

Each of these methodologies provided a framework for the calculation of the phonon spectrum of a system with known defect geometries. However, the works provide limited insight into the ways in which material phonon spectra shift as defect parameters are altered, a field that has primarily been studied through numerical or physical experiments. For example, Feldman et al [4] studied the spectrum of germanium under different silicon concentrations, or silicon defect densities. The authors observed two defect-induced changes to the Raman Spectrum. First, they noted a new peak at approximately 400 cm^{-1} for silicon concentrations higher than 1%. They also noted a red shift in the peak at 300 cm^{-1} . Feldman et al postulated that the new peak was due to the relatively low mass of silicon compared to germanium, and the shift of the lower frequency mode was likely induced by the potential between nearest-neighbor silicon-silicon bonds.

More recent works continue to utilize Raman Spectroscopy to determine the spectral properties of various materials with defects [2,5,6]. As discussed in Section 1, Luo et al [2] were able to measure the spectra of graphene samples with different concentrations of hydrogen atoms. Luo et al noted two spectral changes as defect density was increased: a new peak at 1620 cm^{-1} and a change in the relative intensity between the peaks at 1330 cm^{-1} and 1580 cm^{-1} .

It is difficult to determine the exact composition of the samples measured through Raman Spectroscopy. Simulation, however, allows for the user to create an exact atomic composition for each test specimen. Furthermore, as computational power continues to increase, additional realism may be added to atomic simulations

to better represent complex geometries, large system sizes, and complex potentials. Thus numerical experiments, or simulations, are a popular alternative to physical measurements in the study of defect dynamics. Zhang et al [18], for example, used molecular dynamic simulations to determine the phonon density of states, and then the Green-Kubo method to compute the thermal conductivity of graphene with vacancies. By iteratively performing slightly modified simulations, the authors were able to determine how the thermal conductivity of graphene changes with an increased vacancy concentration randomly dispersed through the sample. The authors were able to control the exact defect density in each iteration to generate a graphical relation between vacancy concentration and specific heat.

1.1.2 Microstructure and Continuum Analyses

With the advent of “smart” materials, and an increase in computational power, atomic lattice methodologies are commonly applied to microstructure or even continuum-level systems to gain better understandings of macro-level phenomena in materials [12, 19–22]. For example, Nolde et al [21] developed a methodology for examining vibration modes through a two-dimensional square lattice composed of elastic strings. By employing lattice dynamics, the authors were able to calculate high frequency modes, whereas prior approaches were only accurate for wavelengths larger than the micro-structure of the material. Slepyan [20] modeled crack propagation through a periodic lattice, and demonstrated that “bond mass,” or continuous mass, can be used to represent porous and fiber-reinforced materials. Slepyan

showed the relative inaccuracy of the concentrated mass assumption in predicting the speed of crack propagation.

The primary differences between a micro-structure or continuum-level model and an atomic model are the connectivity and the potential between nodes. In the models of Nolde et al [21] and Slepyan [20], the connectivity extends no farther than next-nearest neighbors, whereas atomic lattice interactions are typically assumed to be farther reaching. Furthermore, micro-structure or continuum-level systems have elastic interactions, whereas atomic interactions are quantum-based in nature. The methodology proposed in this work may be applied to any system that can be modeled as a periodic lattice, regardless of connectivity or interaction potential. Therefore, the formulae developed in Section 2 are equally as relevant to continuum-level models containing defects as they are to atomic models.

The design of defects or disorder at the continuum level has become increasingly popular with the growth of phononic or metamaterials [11]. Phononic materials are often modeled as periodic systems in which one or more degrees of freedom has a dissimilar geometry, mass, or elastic potential. Wave propagation within the system can then be manipulated through the alteration of these dissimilarities, or defects. For instance, Theocharis et al [22] developed a systematic method for analyzing the stability of localized modes in continuum-level periodic systems, namely granular crystals. They studied continuum-scale grains and developed simple matrices to manipulate the pristine system into one containing defective grains of dissimilar masses, radii, or elastic moduli. The matrix equations were derived assuming one-dimensional chains of uniform grains interacting only with their nearest neighbors.

Through their approach, they were able to demonstrate that a single defect produces a family of localized modes in anharmonic lattices. In later works Boechler and Theocharis along with others applied their theoretical methodology and experimental setup to develop acoustic wave rectifiers [23] and tunable acoustic filters [24] within one dimensional chains of spheres. Sigalas [12] used lattice dynamic equations to study defects in a two-dimensional supercell composed of solid cylinders. Sigalis studied a pristine system that contained an acoustic band gap, and then introduced line defects to the system. These line defects acted as waveguides for frequencies within the forbidden range of the pristine structure. Each of these systems, at least under the harmonic approximation, could be calculated with the methodology proposed herein.

1.1.3 Structural Health Monitoring in Truss Networks

The challenges of finding and mitigating the effects of damage in engineered structures have also motivated the development of evaluation and testing methods that share similar features with the spectroscopic studies of defective materials. Structural health monitoring (SHM), or the ability to continuously monitor a system for damage, has become an increasingly popular area of study since the 1970s. Successful implementation of SHM has the invaluable benefit of preventing catastrophic failures in large-scale systems. Furthermore, SHM allows users to diminish, or in some cases eliminate, regularly scheduled safety checks. Several review articles have been published about various structural health monitoring, or damage locating

methodologies [13, 25, 26]. Interestingly, despite the rich history of damage locating methodologies at the macro level, there is no single method, or even family of methods, that has emerged as the preferred approach. Doebling et al [25] separate their 250 referenced works into 9 unique categories, listing benefits and shortcomings for each family of approaches. One common obstacle in SHM, is the accuracy of the frequency measurements, particularly in noisy environments.

This work is primarily related to the “Matrix Updating” or “Model Updating” methodologies described in [13], which modify the dynamical or stiffness matrices for defect-free configurations to account for the effects of defects or damage. Kabe [15] and Cobb and Liebst [27] developed approaches for altering the stiffness matrices of structural systems to account for the structural response due to damage. Kabe’s model modified the stiffness matrix of a perfect structure by a so-called adjustment matrix. Cobb and Liebst hypothesized that the product of damage and lattice geometry matrices could result in the defective truss stiffness matrix. In both works the extensive interaction matrices were only computed a single time for the pristine, defect-free system. Then the measured frequency response of the structure was utilized to calculate the defective stiffness matrix. In [15] and [27], the respective authors assume that there exists a linear operator to transform a pristine stiffness matrix into a defective matrix, and using this assumption, algorithms for approximating defect locations based on modal measurements were discussed. In this work, I derive the exact form of this operator for periodic systems. The operator is then used to study the effects of various defect types on the defective system modes.

One concern, presented in [26], about model updating methodologies is that

the damage locating algorithms rely heavily upon accurate frequency measurements as well as the accuracy of the numerical model, when compared to the physical structure. Thus if a physical truss-structure is built in such a way that the pristine stiffness matrix is not representative of the initial system, then the damage finding algorithms may not locate damage correctly. However, the methodology proposed herein is solely applied to numerical models, and the purpose is to develop relations between defect properties and modal shifts, not to locate damage. Thus this criticism is not a concern within the scope of this thesis.

Chapter 2: Methodology

In this section linear operators are derived that transform a pristine, defect-free lattice into a defective state. Through the operator methodology, the extensive pristine lattice need only be computed a single time, but the phonon spectrum for any single defect or combination of defects may be computed using simple, linear algebra. The present developments are intended to be general for lattices across all scales. Section 2.1 presents the general formulas for the operator method, which may be applied to any periodic lattice. Then details are filled in for central force pair potentials or linear elastic truss members in Section 2.2.2 and for many-body, non-linear interatomic potentials modeled with the Embedded Atom Method in Section 2.2.3. These models represent just two of the infinitely many interaction potentials that may be modeled using this method.

2.1 Overview

Consider an n -dimensional lattice. The lattice is constructed from a space-filling periodic unit cell containing N nodes. The vibration frequencies or phonon modes of the lattice ($\omega_i \in \mathbb{R}$ for stable systems, or $\omega_i \in \mathbb{C}$ for unstable systems) can

be computed through the eigenvalue problem

$$\sum_{i=1}^{nN} \omega_i^2 \boldsymbol{\chi}_i \otimes \boldsymbol{\chi}_i = \mathbf{M}^{-1} \mathbf{D} \quad (2.1)$$

where $\mathbf{D} \in \mathbb{C}^{nN \times nN}$ is the dynamical matrix, $\mathbf{M} \in \mathbb{R}^{nN \times nN}$ is the mass matrix, and $\boldsymbol{\chi}_i \in \mathbb{C}^{nN}$ are the corresponding eigenvectors to each eigenvalue ω_i^2 . The symbol \otimes is used to denote a tensor product between two vectors. Here, the mass matrix is a compilation of either nodal or continuous masses, and the dynamical matrix contains all information about geometric and kinematic relations between nodes.

The problem statement is as follows: Find $\mathbf{A} \in \mathbb{C}^{nN \times nN}$ and $\mathbf{B} \in \mathbb{R}^{nN \times nN}$ such that the spectrum of the **defective** lattice can be directly computed from the pristine system through

$$\sum_i \omega_{di}^2 \boldsymbol{\chi}_{di} \otimes \boldsymbol{\chi}_{di} = \mathbf{B} \mathbf{M}_p^{-1} \mathbf{A} \mathbf{D}_p \quad (2.2)$$

The script “*p*” is used to indicate quantities associated with the pristine lattice, and “*d*” the defective lattice. \mathbf{A} and \mathbf{B} may be interpreted as operators that map the pristine dynamical and mass matrices into their respective “defect space”. A “defect” can be embodied by the interactions between nodes, the mass of a single node, or some combination of both. Thus a defect in this formulation may be constructed from one or more a) strengthened, weakened, removed, added, and/or reoriented interactions among the nodes of a lattice, or b) changes to the mass of one or more nodes. These two defect classifications have been previously used to explain

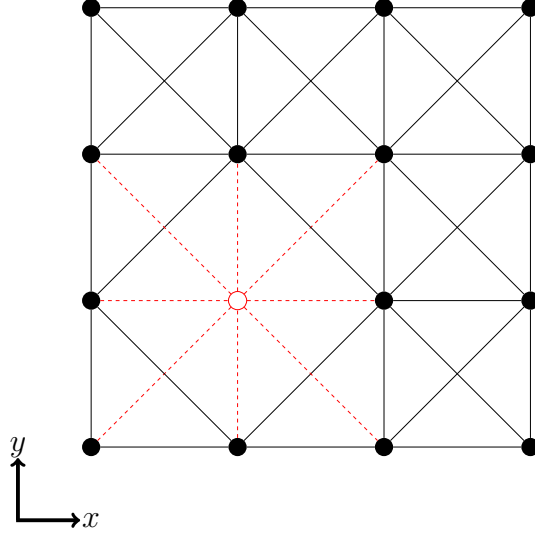


Figure 2.1: Single vacancy in a lattice. The dashed lines are the four nearest neighbor interactions and the eight next-nearest neighbor interactions of a single node in the xy -plane. In the event of a vacancy, each of the red interactions would be removed from the lattice.

defect-induced spectral changes in the experimental work [4]. As an example of the application of bond or mass defects, in a pristine simple cubic lattice with nearest and next-nearest neighbor interactions, a point vacancy is usually considered as the removal of a single node. Here, the vacancy is represented as the removal of the 6 nearest neighbor and 12 next-nearest neighbor interactions involving the missing node, and the removal of the nodal mass, as seen in Fig. 2.1. In similar ways, other types of defects may be constructed, for instance, for interstitial and substitutional point defects, and even line, plane, and volume defects.

Using this method, the dynamical matrix of a defect can be composed by the removal, modification, or addition of a single interaction at a time. The index j is therefore introduced to enumerate each interaction that participates in the defect. Our principal postulate means that operators of the form $\Delta_j \in \mathbb{C}^{nN \times nN}$ represent the defect contribution of a single interaction, and the defective dynamical matrix

\mathbf{D}_d may be obtained through systematically altering each individual interaction through the summation

$$\mathbf{D}_d = \mathbf{D}_p - \sum_j \mathbf{\Delta}_j \quad (2.3)$$

where $\sum_j \mathbf{\Delta}_j$ is similar to the operator $\mathbf{\Lambda}$ described by [9].

Multiplying the right-hand side of (2.3) by $\mathbf{D}_p^{-1}\mathbf{D}_p$ and factoring yields

$$\mathbf{D}_d = \mathbf{A}\mathbf{D}_p \quad (2.4)$$

where

$$\mathbf{A} = \mathbf{D}_d\mathbf{D}_p^{-1} = \mathbf{I} - \left(\sum_j \mathbf{\Delta}_j \right) \mathbf{D}_p^{-1} \quad (2.5)$$

and \mathbf{I} is the $nN \times nN$ identity matrix. While the inversion of the pristine dynamical matrix in (2.5) can be computationally expensive for very large unit cells, the inverse need only be calculated once, and used reiteratively to calculate multiple defect structures within the lattice.

The terms in \mathbf{A} clearly depend on the structure of the host lattice and the structure of each defect. Eq. (2.5) is a general result that only requires the effect of the defective interactions on the dynamical matrix to be additive. This will be further discussed in Section 2.2.1. It is independent of the type of defect and the structure of the pristine lattice. However, under special cases, when the following condition holds

$$\mathbf{\Delta}_m\mathbf{D}_p^{-1}\mathbf{\Delta}_n = \mathbf{0} \quad (2.6)$$

for $m \neq n$, the lattice operator can be constructed from

$$\mathbf{A} = \prod_j \mathbf{A}_j \quad (2.7)$$

where

$$\mathbf{A}_j = \mathbf{I} - \Delta_j \mathbf{D}_p^{-1} \quad (2.8)$$

The condition (2.6) is geometric in nature. The types of lattices for which it is true include five of the primary lattice systems: triclinic, monoclinic, orthorhombic, tetragonal, and cubic, with nearest-neighbor pair potentials. Thus (2.7) is applicable to many monatomic crystals and their alloys. Greater details of (2.6) are in Appendix A. When the orthogonality condition (2.6) is not satisfied, (2.5) should be used to construct complex defects.

It is noted that the contribution of a single interaction to the dynamical matrix is zero everywhere except in the columns and rows corresponding to the nodes spanned by the defective interaction. Let η be the number of nodes; for instance, $\eta = 2$ for the defect composed of a single pair interaction between two nodes r and

defined to represent the product. Namely, \mathbf{A}_j in (2.8) can be written as

$$\mathbf{A}_j = \mathbf{I} - \begin{bmatrix} 0 & \cdots & 0 \\ \vdots & \ddots & \vdots \\ 0 & \cdots & 0 \\ \hline & \boldsymbol{\alpha}_j & \\ \hline 0 & \cdots & 0 \\ \vdots & \ddots & \vdots \\ 0 & \cdots & 0 \end{bmatrix} \quad (2.10)$$

such that $\boldsymbol{\alpha}_j$ is the non-trivial portion of the defect operator. Thus, knowing the terms in $\boldsymbol{\alpha}_j$ is sufficient for determining each \mathbf{A}_j .

Finally, a defect may also manifest in the mass matrix, for instance due to impurities in material lattices, or a damaged truss element in an engineered structure. Similar to (2.4), the defective mass matrix (\mathbf{M}_d) can be computed directly from the mass matrix of the pristine lattice \mathbf{M}_p

$$\mathbf{M}_d = \mathbf{B}\mathbf{M}_p \quad (2.11)$$

If mass is assumed to be concentrated at the system nodes, as in atomic lattices, the mass matrix is diagonal, and the mass defect operator \mathbf{B} is a diagonal matrix

consisting of the ratio of defective mass to pristine mass [22]

$$\mathbf{B}_k = \frac{\mu_k}{m_k} \mathbf{1} \quad (2.12)$$

where μ_k is the mass of the k th node in the defective lattice, m_k is the mass of the k th node in the pristine lattice, and $\mathbf{1}$ is the $n \times n$ identity matrix. In Section 3.2.3, a similar operator will be introduced for systems with consistent mass, or bond mass [20], for applications involving space truss structures.

2.2 Defect Operator Derivation

To demonstrate the calculation method explicitly, some assumptions are needed to restrict the possible forms of the dynamical matrix \mathbf{D}_p . The assumptions used in this section are two-fold. The first requires the potential energy in the lattice to be additively decomposable according to individual interactions, as discussed in Section 2.2.1. The second makes an assumption about the form of the potential energy. Section 2.2.2 invokes the use of a central force potential, and Section 2.2.3 uses the Embedded Atom Method, or EAM potentials.

2.2.1 Additive Potential Energy

The first assumption stems from the realization that the dynamical matrix is the Fourier transform of the Hessian. As such, it is proportional to a second derivative of the interaction potential energy with respect to state variables. The interaction potential, which can be in the form of harmonic potentials, central-force

potentials, and/or empirical many body potentials, can be separated into distinct sets of additive terms with respect to interaction types. Types may be defined by interaction distance, for instance by nearest neighbor or next-nearest neighbor distances, or they may be defined by bond order, such as pair, angle and dihedral contributions, or even by the chemical nature of the interaction such as London dispersion, Coulomb electrostatics, and short-ranged covalent bonds. The potential energy in atomic lattices and truss structures are additively decomposable in this way. The exception to this is quantum mechanics-based approaches, such as density functional theory, that define energy contributions according to the electronic kinetic energy, the energy due to an externally applied field, and an exchange-correlation energy. Insofar as the present developments are considered for atomic lattices, the present discussions are focused solely on molecular modeling techniques that employ classical energy potentials.

I limit the present discussion to an additive decomposition of the energy into b different interaction types. Thus, the dynamical matrix is separable into dynamical matrices indexed using the script β in $\mathbf{D}^{(\beta)}$,

$$\mathbf{D} = \sum_{\beta=1}^b \mathbf{D}^{(\beta)} \quad (2.13)$$

Hence (2.1) becomes

$$\sum_i \omega_i^2 \boldsymbol{\chi}_i \otimes \boldsymbol{\chi}_i = \mathbf{M}^{-1} (\mathbf{D}^{(1)} + \mathbf{D}^{(2)} + \dots + \mathbf{D}^{(b)}) \quad (2.14)$$

As a consequence of this assumption, the problem statement may be re-expressed more specifically as: Find $\mathbf{A}^{(\beta)} \in \mathbb{C}^{nN \times nN}$ and $\mathbf{B} \in \mathbb{R}^{nN \times nN}$ for all $\beta \in [0, b]$ such that, when (2.14) holds for the pristine lattice, the spectrum of the defective lattice can be obtained from

$$\sum_i \omega_{di}^2 \chi_{di} \otimes \chi_{di} = \mathbf{B} \mathbf{M}_p^{-1} (\mathbf{A}^{(1)} \mathbf{D}_p^{(1)} + \mathbf{A}^{(2)} \mathbf{D}_p^{(2)} + \dots + \mathbf{A}^{(b)} \mathbf{D}_p^{(b)}) \quad (2.15)$$

This implies that a defect can be modeled through a modification to the mass \mathbf{M} and numerous dynamical matrices $\mathbf{D}_p^{(\beta)}$ of the pristine, reference lattice. Each separated dynamical matrix $\mathbf{D}_p^{(\beta)}$ can be interpreted as an individual network of interactions, until the dynamical matrices are added together in Eq. (2.15). Thus (2.8) can be applied to each individual system as

$$\mathbf{A}^{(\beta)} = \mathbf{I} - \left(\sum_j \Delta_j^{(\beta)} \right) \mathbf{D}_p^{(\beta)-1} \quad (2.16)$$

when decomposition by interaction-type is required. As seen with (2.6), the geometry of the lattice creates the special condition that

$$\Delta_m^{(\beta)} \mathbf{D}_p^{(\beta)-1} \Delta_n^{(\beta)} = \mathbf{0} \quad (2.17)$$

for all $m \neq n$. Details of this condition are described in Appendix A. With the separation by interaction type, (2.17) holds for systems with farther-reaching interactions than nearest-neighbor. The separation into individual dynamical matrices $\mathbf{D}_p^{(\beta)}$ will be utilized in Section 3.2 to explore two-dimensional rectangular lattices

with nearest neighbor and next-nearest neighbor interactions. Analogous to (2.7), this enables (2.16) to be cast in a much more convenient form as

$$\mathbf{A}^{(\beta)} = \prod_j \mathbf{A}_j^{(\beta)} \quad (2.18)$$

Thus the defect operator may be constructed by multiple interactions, as shown in (2.7), and by interaction type.

2.2.2 Central Forces

While the general formulations presented thus far make no assumptions about the form of the interaction potential, other than being additively decomposable as discussed in Section 2.2.1, in this section all equations will assume central-force pair potentials to make the descriptions specific and relevant for space truss structures as well as certain kinds of atomic lattices.

2.2.2.1 Lattice Dynamical Equations

Consider the n dimensional lattice of Section 2.1 with a space-filling periodic unit cell. Each unit cell is indexed by $l \in \mathbb{Z}$ and contains N nodes $k \in (1, 2, \dots, N)$. The lattice vectors are $\mathbf{a}_\lambda \in \mathbb{R}^n$, where $\lambda \in \mathbb{Z}$ indexes the n lattice vectors. The lattice vectors are defined by $\mathbf{a}_\lambda = \sum_\alpha a_{\lambda\alpha} \hat{\mathbf{n}}_\alpha$, where $\alpha \in \mathbb{Z}$ is for n Cartesian directions, and $\hat{\mathbf{n}}_\alpha \in \mathbb{R}^n$ are the Cartesian unit vectors.

The location of the l th unit cell is defined by $\mathbf{x}^l \in \mathbb{R}^n$, relative to a reference frame centered at $\mathbf{x}^0 \in \mathbb{R}^n$ via the relative position vector $\mathbf{r}^{l0} = \mathbf{x}^l - \mathbf{x}^0$. Simi-

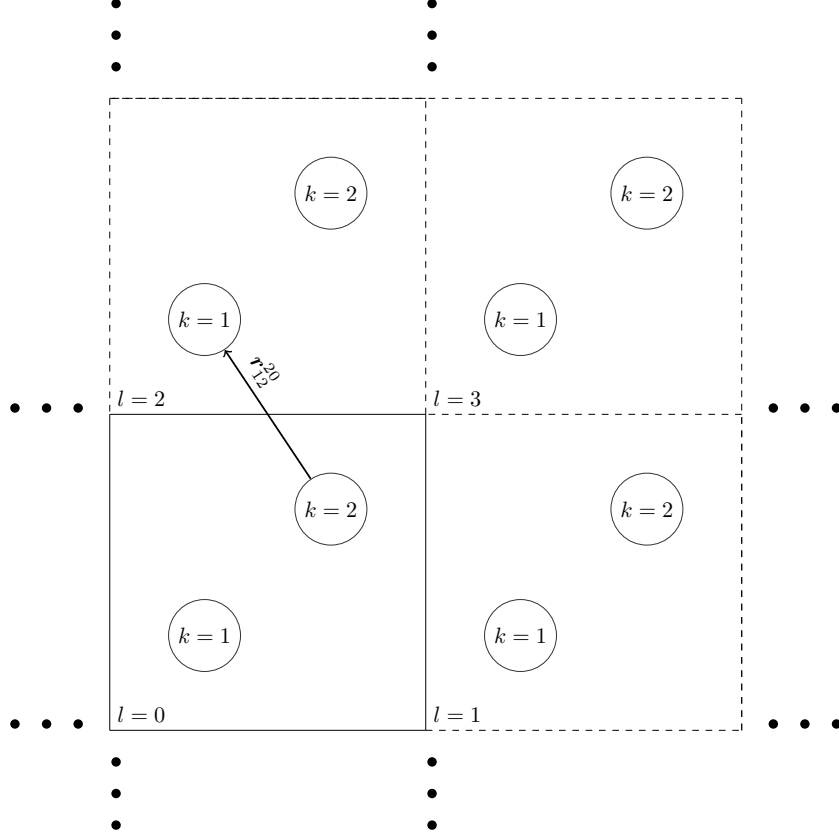


Figure 2.2: Schematic of periodic boundary conditions applied to a unit cell with two unique nodes. The vector between the second node in the reference unit cell and the first node in the second unit cell (\mathbf{r}_{12}^{20}) is shown.

larly, the location of the k th node in the l th unit cell is given by \mathbf{x}_k^l . Thus the position of any node k in unit cell l relative to any other node k' in unit cell l' is defined as $\mathbf{r}_{kk'}^{ll'} = \mathbf{x}_k^l - \mathbf{x}_{k'}^{l'}$ and the corresponding unit vector is $\hat{\mathbf{n}}_{kk'}^{ll'} = \mathbf{r}_{kk'}^{ll'} / |\mathbf{r}_{kk'}^{ll'}|$. Moreover, displacement $\mathbf{u}_k^l \in \mathbb{C}^n$ is also similarly defined. The real part of the displacement, $\Re(\mathbf{u}_k^l)$, is the spatial displacement, while the imaginary part, $\Im(\mathbf{u}_k^l)$, contains information about the phase.

Each of the N nodes in the unit cell has an associated displacement $\mathbf{u}_k^l(t)$,

which is written as a periodic function using Blochs theorem [28] as

$$\mathbf{u}_k^l(t) = \boldsymbol{\chi}_k e^{-i\omega t} e^{i\mathbf{G}\cdot\mathbf{r}^{l0}} \quad (2.19)$$

where $\boldsymbol{\chi}_k \in \mathbb{C}^n$ is the amplitude of vibration for node k , ω is the frequency of vibration, and $\mathbf{G} \in \mathbb{R}^n$ is a wave-vector [29].

The interaction force between the k th node of the l th unit cell, and the k' th node of the l' th cell is defined as (no sum)

$$\mathbf{F}_{kk'}^{ll'} = \phi_{kk'}^{ll'} \mathbf{v}_{kk'}^{ll'} (\mathbf{u}_{k'}^{l'} - \mathbf{u}_k^l) \quad (2.20)$$

where

$$\mathbf{v}_{kk'}^{ll'} = \hat{\mathbf{n}}_{kk'}^{ll'} \otimes \hat{\mathbf{n}}_{kk'}^{ll'} \quad (2.21)$$

such that $\mathbf{v}_{kk'}^{ll'} \in \mathbb{R}^{n \times n}$ is the direction cosine between the k th node in the reference cell and the k' th node in the l' th unit cell which is a measure of the relative orientation of the two nodes. $\phi_{kk'}^{ll'}$ is the force constant of the interaction in units of force per length.

The net force on the k th node in the l th unit cell is then

$$\mathbf{F}_k^l = \sum_{l'k'} \phi_{kk'}^{ll'} \mathbf{v}_{kk'}^{ll'} (\mathbf{u}_{k'}^{l'} - \mathbf{u}_k^l) \quad (2.22)$$

where the sum is taken over all nodes k' in unit cells l' (including $l' = 0$) that interact with node k in unit cell l . Additionally, $\phi_{kk'}^{ll'} = 0$ when $k = k'$ and $l = l'$.

Here, I have followed conventions for atomic lattices, by taking the summation over *nodes*, whereas in earlier summations, such as in (2.3), the sums were taken over *interactions*. In atomic lattices with periodic boundary conditions, each node may interact with infinitely many other nodes, and the sum would consequently have infinitely many terms. However, it is customary to limit the interactions to a neighborhood around each node.

I will use lumped masses in the descriptions that follow. Section 3.2.3 describes the extensions to consistent mass representations. Defining the mass of the k th node in the l th cell as $m_k^l \in \mathbb{R}$, the equation of motion of the k th node in unit cell l is then

$$m_k^l \ddot{\mathbf{u}}_k^l = \sum_{l'k'} \phi_{kk'}^{ll'} \mathbf{v}_{kk'}^{ll'} (\mathbf{u}_{k'}^{l'} - \mathbf{u}_k^l) \quad (2.23)$$

The periodicity of the cell can be used to reduce the number of atoms represented by the index k to only those atoms in the reference cell $l = 0$,

$$m_k \ddot{\mathbf{u}}_k = \sum_{l'k'} \phi_{kk'}^{l'l'} \mathbf{v}_{kk'}^{l'l'} (\mathbf{u}_{k'}^{l'} - \mathbf{u}_k) \quad (2.24)$$

where the superscript $l = 0$ is not shown for notational simplicity.

Substituting (2.19) into (2.24) then gives

$$m_k \omega^2 \boldsymbol{\chi}_k - \sum_{l'k'} \phi_{kk'}^{l'l'} \mathbf{v}_{kk'}^{l'l'} \left(\boldsymbol{\chi}_k - \boldsymbol{\chi}_{k'} \exp(i\mathbf{G} \cdot \mathbf{r}^{l'0}) \right) = 0 \quad (2.25)$$

Comparing (2.25) with (2.1), it can be seen that the mass matrix for a system with

point masses is a diagonal matrix of the nodal masses m_k

$$\mathbf{M}_k = m_k \mathbf{1} \quad (2.26)$$

The dynamical matrix is composed of $N \times N$ sub-matrices $\mathbf{D}_{kk'} \in \mathbb{C}^{n \times n}$

$$\mathbf{D} = \begin{bmatrix} \mathbf{D}_{11} & \mathbf{D}_{12} & \cdots & \mathbf{D}_{1N} \\ \mathbf{D}_{21} & \mathbf{D}_{22} & \cdots & \mathbf{D}_{2N} \\ \vdots & \vdots & \ddots & \vdots \\ \mathbf{D}_{N1} & \mathbf{D}_{N2} & \cdots & \mathbf{D}_{NN} \end{bmatrix} \quad (2.27)$$

When nodes do not interact with their periodic images, i.e. when the k th node in the reference unit cell does not interact with the k th node in any other unit cell l' , the sub-matrices \mathbf{D}_{kk} located along the diagonal can be derived from the second term in (2.25) as

$$\mathbf{D}_{kk} = \sum_{l'k'} \phi_{kk'}^{l'} \mathbf{v}_{kk'}^{l'} \quad (2.28)$$

The general form of (2.28) accounting for interactions between any two nodes in the system is

$$\mathbf{D}_{kk} = \sum_{l'k'} \phi_{kk'}^{l'} \mathbf{v}_{kk'}^{l'} \left(1 - \delta_{kk'} \exp(i\mathbf{G} \cdot \mathbf{r}^{l'0}) \right) \quad (2.29)$$

where $\delta_{kk'}$ is a Kronecker delta. Similarly, the off-diagonal components $\mathbf{D}_{kk'}$ for $k \neq k'$ can be derived from the second term in (2.25) as

$$\mathbf{D}_{kk'} = \sum_{l'} \phi_{kk'}^{l'} \mathbf{v}_{kk'}^{l'} \exp(i\mathbf{G} \cdot \mathbf{r}^{l'0}) \quad (2.30)$$

Eqs. (2.29) and (2.30) may be combined into one general equation to solve for each sub-matrix, $\mathbf{D}_{kk'}$, by utilizing l'' and k'' to enumerate all nodes k'' in unit cells l'' that interact with the k th node in the reference unit cell

$$\mathbf{D}_{kk'} = \sum_{l''k''} \phi_{kk''}^{l''} \mathbf{v}_{kk''}^{l''} \left(\delta_{kk'} - \delta_{k'k''} \exp \left(i\mathbf{G} \cdot \mathbf{r}^{l''0} \right) \right) \quad (2.31)$$

Based on (2.31) the configuration-dependent information about each interaction (such as orientation, length, and location) can be factored into a sub-matrix $\boldsymbol{\psi}_{kk'k''}^{l''} \in \mathbb{C}^{n \times n}$ such that

$$\mathbf{D}_{kk'} = \sum_{l''k''} \phi_{kk''}^{l''} \boldsymbol{\psi}_{kk'k''}^{l''} \quad (2.32)$$

where

$$\boldsymbol{\psi}_{kk'k''}^{l''} = \mathbf{v}_{kk''}^{l''} \left(\delta_{kk'} - \delta_{k'k''} \exp \left(i\mathbf{G} \cdot \mathbf{r}^{l''0} \right) \right) \quad (2.33)$$

Thus, the force information is solely contained in $\phi_{kk''}^{l''}$ and the kinematic information is contained in $\boldsymbol{\psi}_{kk'k''}^{l''}$. In indicial form, the terms in the dynamical matrix may be written as

$$D_{kk'\alpha\alpha'} = \sum_{l''k''} \phi_{kk''}^{l''} \hat{\mathbf{n}}_{\alpha}^T \boldsymbol{\psi}_{kk'k''}^{l''} \hat{\mathbf{n}}_{\alpha'} = \sum_{l''k''} \phi_{kk''}^{l''} \psi_{kk'k''\alpha\alpha'}^{l''} \quad (2.34)$$

The dynamical and mass matrices can be substituted into (2.14) to find the system modes for the lattice. Dispersion curves can be calculated by plotting the modes as a function of wave-vector \mathbf{G} along the crystal high symmetry lines [29].

2.2.2.2 Defect Operators for Central Forces

The kinematic term in the dynamical matrix, $\boldsymbol{\psi}_{kk'k''}^{l''}$, can be written as a function of an interaction in a basic reference configuration $\boldsymbol{\xi}_{kk'k''}^{l''} \in \mathbb{C}^{n \times n}$ and transformations through an $O(3)$ rotation operator $\mathbf{R}_{kk''}^{l''} \in \mathbb{R}^{n \times n}$ such that

$$\boldsymbol{\psi}_{kk'k''}^{l''} = \mathbf{R}_{kk''}^{l''} \boldsymbol{\xi}_{kk'k''}^{l''} \mathbf{R}_{kk''}^{l''T} \quad (2.35)$$

where $\boldsymbol{\xi}_{kk'k''}^{l''}$ is the kinematic term for the pristine, reference lattice, and is calculated as

$$\boldsymbol{\xi}_{kk'k''}^{l''} = \mathbf{v}_{kk''}^{l''} \left(\delta_{kk'} - \delta_{k'k''} \exp \left(i \mathbf{G} \cdot \mathbf{r}^{l''0} \right) \right) \quad (2.36)$$

where $\mathbf{v}_{kk''}^{l''}$ is the dyadic product of the vectors drawn between nodes in the pristine configuration. $\mathbf{R}_{kk''}^{l''}$ rotates the reference interaction in the pristine lattice into its defective configuration. Note that a stretch operator to account for changes in bond length is not needed since $\boldsymbol{\psi}_{kk'k''}^{l''}$ is independent of bond length. Rather, bond length would likely alter the interaction potential, $\phi_{kk'}^{l''}$. The geometric changes associated with relaxation may therefore be represented using transformation (2.35) under the assumption that nodes remain in the same unit cells after relaxation. In the absence of relaxation, I presently take $\mathbf{R}_{kk''}^{l''}$ to be the identity matrix.

Defining a scalar damage coefficient $q_{kk''}^{l''} \in \mathbb{R}$, which accounts for changes to the potential energy of an interaction due to a defect, the damage factor is multiplied

to the interaction potential $\phi_{kk''}^{l''}$ for one interaction at a time. Thus (2.32) becomes

$$\mathbf{D}_{kk'} = \sum_{l''k''} q_{kk''}^{l''} \phi_{kk''}^{l''} \boldsymbol{\psi}_{kk'k''}^{l''} \quad (2.37)$$

A value of 1 for the coefficient represents an unchanged interaction potential, a smaller value indicates a weakened interaction, and a larger value represents a strengthened interaction. In the atomic analogue of this problem, $q_{kk''}^{l''}$ adjusts the interatomic potential between the k th atom in the reference unit cell and the k'' th atom in the l'' th unit cell. A substitutional defect may require $q_{kk''}^{l''} > 1$, for instance due to the different electronegativity of the substitute atom in the host lattice. Traditionally, a void could be created by setting the damage coefficients of numerous interactions to zero, $q_{kk''}^{l''} = 0$, however, Montroll and Potts in [7] recommend using a damage coefficient of $q_{kk''}^{l''} > 1$ to model a vacancy in order to simulate relaxation of neighboring atoms into the hole created by the missing atom. In general, the notion of a broken bond would be simulated by a coefficient whose value is zero. Continuous values of $q_{kk''}^{l''}$ would be appropriate for truss structures experiencing variable fatigue, wear, environmental conditions, or predesigned use of a different truss member.

In a pristine lattice we have $q_{kk''}^{l''} = 1$ and $\mathbf{R}_{kk''}^{l''} = \mathbf{1} \forall k, k'', l''$, and the pristine dynamical matrix follows from (2.35) and (2.37)

$$\mathbf{D}_{p_{kk'}} = \sum_{l''k''} \phi_{kk''}^{l''} \boldsymbol{\xi}_{kk'k''}^{l''} \quad (2.38)$$

Using (2.35), the defective dynamical matrix \mathbf{D}_d in the absence of bond rotation is

$$\mathbf{D}_{d_{kk'}} = \sum_{l''k''} q_{kk''}^{l''} \phi_{kk''}^{l''} \boldsymbol{\xi}_{kk'k''}^{l''} \quad (2.39)$$

which can be rearranged to yield

$$\begin{aligned} \mathbf{D}_{d_{kk'}} &= \sum_{l''k''} \phi_{kk''}^{l''} \boldsymbol{\xi}_{kk'k''}^{l''} - \sum_{l''k''} \phi_{kk''}^{l''} (1 - q_{kk''}^{l''}) \boldsymbol{\xi}_{kk'k''}^{l''} \\ &= \mathbf{D}_{p_{kk'}} - \sum_{l''k''} \phi_{kk''}^{l''} (1 - q_{kk''}^{l''}) \boldsymbol{\xi}_{kk'k''}^{l''} \end{aligned} \quad (2.40)$$

Typically, the number of nodes (or number of interactions) that are influenced by the defect can be assumed to be finite. So a subset of nodes in the vicinity of the defect is defined, and node indices r and r' and the unit cell index s' are used for summations over those nodes. Thus, the defective dynamical matrix becomes

$$\mathbf{D}_d = \mathbf{D}_p - \sum_{r,r',s'} \boldsymbol{\Delta}_{rr'}^{s'} \quad (2.41)$$

and the non-trivial portion of $\boldsymbol{\Delta}_{rr'}^{s'}$, $\mathbf{d}_{rr'}^{s'}$ defined in (2.9) is

$$\mathbf{d}_{rr'}^{s'} = \phi_{rr'}^{s'} (1 - q_{rr'}^{s'}) \begin{bmatrix} \mathbf{v}_{rr'}^{s'} & -\mathbf{v}_{rr'}^{s'} \exp(i\mathbf{G} \cdot \mathbf{r}^{s'0}) \\ -\mathbf{v}_{rr'}^{s'} \exp(i\mathbf{G} \cdot \mathbf{r}^{0s'}) & \mathbf{v}_{rr'}^{s'} \end{bmatrix} \quad (2.42)$$

Finally, (2.42) can be substituted into (2.5) to obtain the defect operator, and (2.10)

becomes

$$\mathbf{A}_{rr'}^{s'} = \mathbf{I} - \begin{bmatrix} 0 & \cdots & 0 \\ \vdots & \ddots & \vdots \\ 0 & \cdots & 0 \\ \hline & & \boldsymbol{\alpha}_{rr'}^{s'} \\ \hline 0 & \cdots & 0 \\ \vdots & \ddots & \vdots \\ 0 & \cdots & 0 \end{bmatrix} \quad (2.43)$$

Eq. (2.43) is the defect operator for a single central force interaction. When used with (2.38) and (2.4), it gives the dynamical matrix of the lattice containing the defect. When more than one interaction constitutes the defect, the defective dynamical matrix (2.4) is then obtained using (2.7) and (2.38), where (2.43) is used reiteratively in (2.7).

2.2.3 Embedded Atom Method

In the embedded atom method (EAM) [30] each atom is modeled as a particle within an electron cloud. This simplification, derived in [31], is based on Density Functional Theory (DFT), in which the nucleus and core electrons of an atom are treated as a single degree of freedom, and the valence electrons are treated as additional degrees of freedom. However, EAM unlike DFT is a classical potential, and therefore does not contain quantum effects. In this work, the atom without the valence electrons will be considered the atom “core” and the valence electrons of

each atom will simply be referred to as “electrons.” The separation between atom cores and electrons is particularly useful in simulating the properties of single crystal metals [32] and alloys [33] because it approximates the cohesive energy of metallic lattices better than pair-potentials.

Using the EAM approach, contributions to the net potential energy of the lattice can be separated into two terms: pair potentials between sets of cores, which are always repulsive in nature, and the “embedding energy” inserting an atom into the electron cloud of the surrounding atoms. The pair potential between the k'' th atom in the l'' th unit cell and the k''' th atom in the l''' th unit cell is defined as $\Phi(r_{k''k'''}^{l''l'''}) \in \mathbb{R}$. The embedding energy term of the k'' th atom in the l'' th unit cell is $\Upsilon(\rho_{k''}^{l''}) \in \mathbb{R}$, where $\rho_{k''}^{l''} \in \mathbb{R}$ is the electron density of the lattice at the site of the atom.

The net energy E associated with a lattice using EAM potentials is a sum over all embedding energy and pair potential terms,

$$E = \sum_{k''l''} \Upsilon(\rho_{k''}^{l''}) + \frac{1}{2} \sum_{k''k''',l''l'''} \Phi(r_{k''k'''}^{l''l'''}) \quad (2.44)$$

where the net electron density at each atom site, $\rho_{k''}^{l''}$, is a sum of the electron densities associated with each pair interaction $\Psi(r_{k''k'''}^{l''l'''}) \in \mathbb{R}$,

$$\rho_{k''}^{l''} = \sum_{k'''}^{l'''} \Psi(r_{k''k'''}^{l''l'''}) \quad (2.45)$$

If two atoms k'' and k''' in unit cells l'' and l''' , respectively are closer together, the

electron density term $\Psi(r_{k''k'''}^{l''l'''})$ is higher since the same number of valence electrons occupy a smaller volume. $\Psi(r_{k''k'''}^{l''l'''})$, therefore, is highly dependent on geometry. However, $\Psi(r_{k''k'''}^{l''l'''})$ is also dependent on the element type involved in the interaction, or more specifically, it is dependent on the number of valence electrons of atoms k'' and k''' . Using (2.45) in (2.44), the electron density potential Υ is a function of the properties of all atoms located within a neighborhood around each node. Thus Υ is a many-body potential.

The force on an atom k in unit cell l is related to the energy function through

$$\mathbf{F}_k^l = -\frac{\partial E}{\partial \mathbf{x}_k^l} \quad (2.46)$$

The pair potentials Φ , electron density terms Ψ , and electron density potentials Υ , vary between materials, and are typically fit to empirical data. For example, Sun et. al. in [34] report the density and energy functions for magnesium shown in Figure 2.3.

The pair potential Φ represents the repulsion between two atom cores, and therefore the energy function is always positive for all values of r , as can be seen in Fig. 2.3. Furthermore, the slope of the curve is always negative since the force between cores is repulsive for all r , and therefore has a positive force \mathbf{F} using Eq. (2.46). Υ , however, represents both electron-electron and core-electron interactions, and thus the slope of Υ is positive for high electron densities, where the repulsive forces between electrons outweigh the attractive forces between electrons and cores, but is negative for lower values of the electron density.

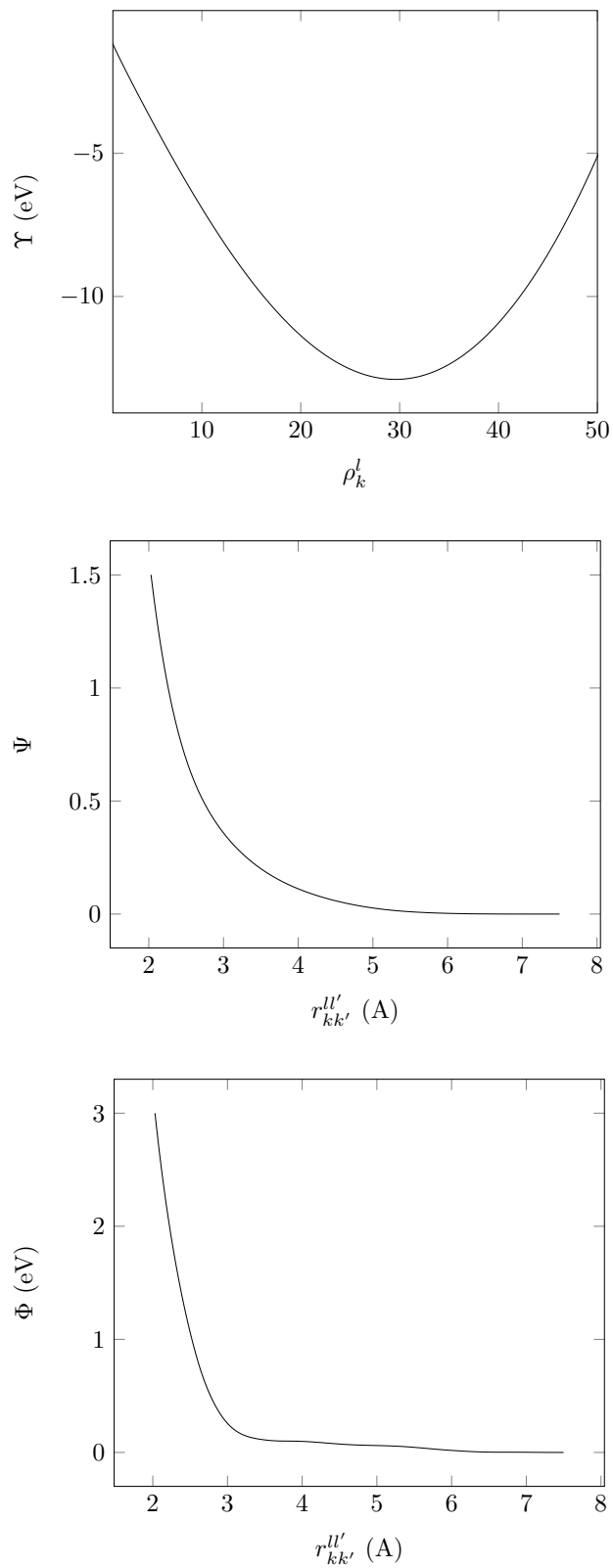


Figure 2.3: The embedded atom method potential functions as reported in [34] for magnesium

The many-body term in the energy equation, along with the non-linear pair-potential result in additional terms in the lattice dynamics equations. Therefore, the lattice dynamic equations are re-derived, and then an approach for using the proposed methodology of Section 2.1 on systems with an EAM potential is outlined.

2.2.3.1 Lattice Dynamics for EAM potentials

In this section the dynamical matrix is derived for systems with EAM potentials. Consider a lattice with L unit cells. In atomic lattices, L is theoretically infinite, but is often simplified to a small set of unit cells within the cutoff distance of the reference unit cell $l = 0$, and the remainder of the infinitely many unit cells are represented through periodic boundary conditions. The Hessian is composed of $NL \times NL$ sub-matrices $\mathbf{H}_{kk'}^{l'l'} \in \mathbb{R}^{n \times n}$, and the dynamical matrix is, by definition, the discrete Fourier transform of the Hessian. Thus, each sub-matrix $\mathbf{D}_{kk'}$ of Eq. (2.27) is simply

$$\mathbf{D}_{kk'} = \sum_{l'} e^{i\mathbf{G} \cdot \mathbf{r}^{l'0}} \mathbf{H}_{kk'}^{0l'} \quad (2.47)$$

where each sub-matrix of the Hessian is calculated through

$$\mathbf{H}_{kk'}^{l'l'} = \frac{\partial^2 E}{\partial \mathbf{x}_k^l \partial \mathbf{x}_{k'}^{l'}} \quad (2.48)$$

the second derivative of the energy with respect to atom coordinates, or so-called state variables.

Substituting (2.45) into (2.44), the first derivative of the energy function can

be evaluated as

$$\frac{\partial E}{\partial \mathbf{x}_k^l} = \sum_{k''k''''l''l''''} \left(\Upsilon'(\rho_{k''}) \Psi'(r_{k''k''''}^{l''l''''}) + \frac{1}{2} \Phi'(r_{k''k''''}^{l''l''''}) \right) \hat{\mathbf{n}}_{k''k''''}^{l''l''''} (\delta_{kk''''} \delta_{l''l''} - \delta_{kk''} \delta_{l''l''''}) \quad (2.49)$$

which may be simplified to

$$\frac{\partial E}{\partial \mathbf{x}_k^l} = - \sum_{k''l''} \left(\left(\Upsilon'(\rho_{k''}) + \Upsilon'(\rho_k^l) \right) \Psi'(r_{kk''}^{l''}) + \Phi'(r_{kk''}^{l''}) \right) \hat{\mathbf{n}}_{kk''}^{l''} \quad (2.50)$$

using the relations $r_{kk''}^{l''} = r_{k''k}^{l''l}$ and $\hat{\mathbf{n}}_{kk''}^{l''} = -\hat{\mathbf{n}}_{k''k}^{l''l}$. Eq. (2.50) is directly related to the force \mathbf{F}_k^l through (2.46).

The components of the Hessian, following (2.48), may be computed by taking the derivative of (2.50) with respect to $\mathbf{x}_{k'}^{l'}$

$$\begin{aligned} \mathbf{H}_{kk'}^{l'l'} &= \sum_{k''k''''l''l''''} (\delta_{k'k''} \delta_{l'l''} - \delta_{k'k''''} \delta_{l'l''''}) \Upsilon''(\rho_{k''}) \Psi'(r_{k''k''''}^{l''l''''}) \Psi'(r_{kk''}^{l''}) \hat{\mathbf{n}}_{k''k''''}^{l''l''''} \otimes \hat{\mathbf{n}}_{kk''}^{l''} \\ &+ \sum_{k''k''''l''l''''} (\delta_{kk'} \delta_{l'l''} - \delta_{k'k''''} \delta_{l'l''''}) \Upsilon''(\rho_k^l) \Psi'(r_{kk''''}^{l''l''''}) \Psi'(r_{kk''}^{l''}) \hat{\mathbf{n}}_{kk''''}^{l''l''''} \otimes \hat{\mathbf{n}}_{kk''}^{l''} \\ &+ \sum_{k''l''} (\delta_{kk'} \delta_{l'l''} - \delta_{k'k''} \delta_{l'l''}) \left(\left(\Upsilon'(r_{k''}^{l''}) + \Upsilon'(r_k^l) \right) \Psi''(r_{kk''}^{l''}) + \Phi''(r_{kk''}^{l''}) \right) \mathbf{v}_{kk''}^{l''} \\ &+ \sum_{k''l''} \frac{\delta_{kk'} \delta_{l'l''} - \delta_{k'k''} \delta_{l'l''}}{r_{kk''}^{l''}} \left(\left(\Upsilon'(\rho_{k''}) + \Upsilon'(\rho_k^l) \right) \Psi'(r_{kk''}^{l''}) + \Phi'(r_{kk''}^{l''}) \right) \left(\mathbf{1} - \mathbf{v}_{kk''}^{l''} \right) \end{aligned} \quad (2.51)$$

which, in turn, may be used in (2.47) to solve for the dynamical matrix.

Once again, the additive potential energy described in Section 2.2.1 can be utilized to isolate the contributions of the pair potentials in matrix $\mathbf{D}^{(1)}$, and the many-bodied electron density term in matrix $\mathbf{D}^{(2)}$. Using (2.51) in (2.47), the

contribution of the pair potentials to the dynamical matrix is

$$\mathbf{D}_{kk'}^{(1)} = \sum_{k''l''} (\delta_{kk'} - \delta_{k'k''} e^{i\mathbf{G}\cdot\mathbf{r}^{0l''}}) \left[\Phi''(r_{kk''}^{0l''}) \mathbf{v}_{kk''}^{0l''} + \frac{1}{r_{kk''}^{0l''}} \Phi'(r_{kk''}^{0l''}) (\mathbf{1} - \mathbf{v}_{kk''}^{0l''}) \right] \quad (2.52)$$

and the contribution of the electron density term is

$$\begin{aligned} \mathbf{D}_{kk'}^{(2)} = & \sum_{k''k'''l''l'''} (\delta_{k'k''} e^{i\mathbf{G}\cdot\mathbf{r}^{0l''}} - \delta_{k'k'''} e^{i\mathbf{G}\cdot\mathbf{r}^{0l'''}}) \Upsilon''(\rho_{k''}^{l''}) \Psi'(r_{k''k'''}^{l''l'''}) \Psi'(r_{kk''}^{0l''}) \hat{\mathbf{n}}_{k''k'''}^{l''l'''} \otimes \hat{\mathbf{n}}_{kk''}^{0l''} \\ & + \sum_{k''k'''l''l'''} (\delta_{kk'} - \delta_{k'k'''} e^{i\mathbf{G}\cdot\mathbf{r}^{0l'''}}) \Upsilon''(\rho_k) \Psi'(r_{kk'''}^{0l''''}) \Psi'(r_{kk''}^{0l''}) \hat{\mathbf{n}}_{kk'''}^{0l''''} \otimes \hat{\mathbf{n}}_{kk''}^{0l''} \\ & + \sum_{k''l''} (\delta_{kk'} - \delta_{k'k''} e^{i\mathbf{G}\cdot\mathbf{r}^{0l''}}) (\Upsilon'(\rho_{k''}^{l''}) + \Upsilon'(r_k)) \Psi''(r_{kk''}^{0l''}) \left[\mathbf{v}_{kk''}^{0l''} + \frac{1}{r_{kk''}^{0l''}} (\mathbf{1} - \mathbf{v}_{kk''}^{0l''}) \right] \end{aligned} \quad (2.53)$$

where superscript $l = 0$ has been eliminated for simplicity. Note that when $\Phi'(r_{kk'}^l) = 0$ for all k, k' , and l , (2.52) is equivalent to (2.31) with $\Phi''(r_{kk'}^l) = \phi_{kk'}^l$. This case corresponds to the assumption that each interaction is at a local energy minimum. The configuration that corresponds to the minimum lattice energy does not necessarily minimize the energy of each individual interaction. In material lattices, this assumption is valid in a fully relaxed system with nearest-neighbor bonds only. In truss structures, the assumption corresponds with a lattice that is stress-free at equilibrium. (2.52) can therefore be interpreted as a more general form of (2.31).

Dynamical matrices (2.52) and (2.53) and mass matrix (2.26) can be used in (2.1) to find the complete set of eigenvalues for each wave-vector \mathbf{G} . The dispersion curves for magnesium calculated using (2.52) and (2.53) are shown in Fig. 2.4. The potential functions of Fig. 2.3 and atomic mass $m = 24.305$ g/mol were used in the

calculation. All derivatives were calculated from the discrete functions presented in [34] using fifth-order Taylor expansions. For instance, the n th value of the first derivative Φ' was computed as

$$\Phi'_n = \frac{\frac{1}{12}\Phi_{n-2} - \frac{2}{3}\Phi_{n-1} + \frac{2}{3}\Phi_{n+1} - \frac{1}{12}\Phi_{n+2}}{\Delta r} \quad (2.54)$$

and the n th value of the second derivative Φ'' was computed through

$$\Phi''_n = \frac{-\frac{1}{12}\Phi_{n-2} + \frac{4}{3}\Phi_{n-1} - \frac{5}{2}\Phi_n + \frac{4}{3}\Phi_{n+1} - \frac{1}{12}\Phi_{n+2}}{(\Delta r)^2} \quad (2.55)$$

where Δr is the difference between successive values of r in the tabulated function. In [34], $\Delta r = .00075 \text{ \AA}$. The fifth order approximations were chosen for increased numerical accuracy as compared to the typical second order approximations.

To verify the accuracy of the derived formulas, the dispersion curves using (2.52), (2.53), and (2.26) in (2.1) are compared with dispersion curves obtained with the General Utility Lattice Program (GULP) [35] in Fig. 2.4. As can be seen, the two calculation approaches are numerically equivalent.

2.2.3.2 Defect Operators for EAM Potential

In the absence of relaxation, it is assumed that defects can alter the lattice dynamic response in one of three ways: through alterations in nodal mass as accounted for in (2.12), strengthened/weakened pair potentials, or alterations in the electron density. Φ_p and Ψ_p are henceforth defined as functions related to the pristine lattice,

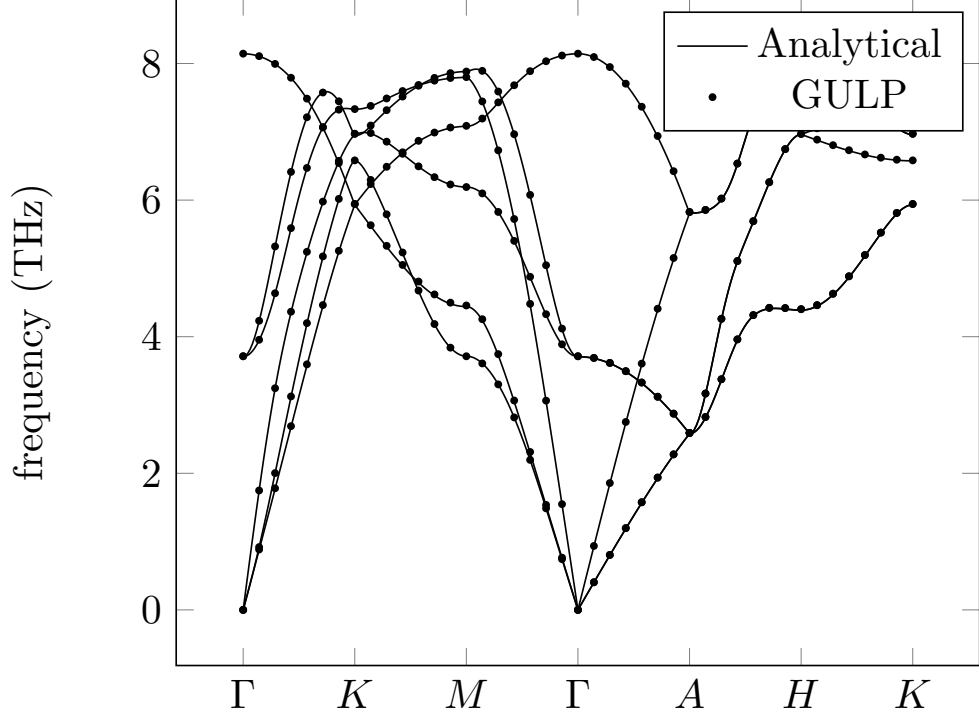


Figure 2.4: Dispersion curves of magnesium using an embedded atom potential. The solid lines are the dispersion curves using (2.26), (2.52), and (2.53) in (2.1), whereas the circular data points were computed using GULP [35]

and Φ_d and Ψ_d are the corresponding functions of the defective lattice. Two linear defect coefficients $q_{kk'}^{ll'}$ and $p_{kk'}^{ll'}$ are defined such that the pristine functions $\Phi_p(r_{kk'}^{ll'})$ and $\Psi_p(r_{kk'}^{ll'})$ are mapped into a defective state through

$$\Phi_d(r_{kk'}^{ll'}) = q_{kk'}^{ll'} \Phi_p(r_{kk'}^{ll'}) \quad (2.56)$$

$$\Psi_d(r_{kk'}^{ll'}) = p_{kk'}^{ll'} \Psi_p(r_{kk'}^{ll'}) \quad (2.57)$$

The electron density in the defective lattice at the k th atom in the l th unit cell is calculated using (2.57) in (2.45) as

$$\rho_{kd}^l = \sum_{k'}^{l'} p_{kk'}^{ll'} \Psi_p(r_{kk'}^{ll'}) \quad (2.58)$$

It is assumed that the electron density potential function Υ does not change in going from the pristine state to the defective state i.e. $\Upsilon \equiv \Upsilon_p \equiv \Upsilon_d$. However the value of the potential $\Upsilon(\rho_k^l)$ at a specific atomic site might change due to alterations in the electron density ρ_k^l at that atom site. The electron density potential of the k th atom in the l th unit cell in the defective state is then

$$\Upsilon(\rho_{kd}^l) = \Upsilon \left(\sum_{k'l'} p_{kk'}^{ll'} \Psi(r_{kk'}^{ll'}) \right) = \Upsilon \left(\rho_k^l - \sum_{k'l'} (1 - p_{kk'}^{ll'}) \Psi(r_{kk'}^{ll'}) \right) \quad (2.59)$$

Using a first order Taylor expansion, (2.59) becomes

$$\Upsilon(\rho_{kd}^l) = \Upsilon(\rho_k^l) - \sum_{k'l'} (1 - p_{kk'}^{ll'}) \Psi(r_{kk'}^{ll'}) \Upsilon'(\rho_k^l) \quad (2.60)$$

or a higher-order Taylor expansion could be used for increased accuracy.

The pristine dynamical matrices and defective dynamical matrices are not shown due to the length of the expressions. The pristine dynamical matrices may be calculated directly through (2.52) and (2.53) using $\Phi = \Phi_p$ and $\Psi = \Psi_p$. Two pair potential defect operators $\Delta^{(1)}$ and $\Delta^{(2)}$ may be derived to compute $D_d^{(1)}$ and $D_d^{(2)}$, respectively. The pair potential defect operator, $\Delta^{(1)}$, may be solved by substituting (2.52) and (2.56) into (2.3). Similarly, the electron density defect operator, $\Delta^{(2)}$, is calculated using (2.53), (2.57), and (2.60) in (2.3).

Chapter 3: Results and Analysis

In this section the developments of Section 2 are applied to problems representative of those encountered in the fields of molecular and structural dynamics. First, I examine 1D and 2D systems under the central force assumption whose simplicity allow the complete matrix expressions to be shown. Finally, the representation of vacancies in a three dimensional lattice with EAM potential is explored in Section 3.3.

3.1 Convergence to the Dilute Defect Limit in a 1D Lattice Chain.

In this section I demonstrate that the operator approach of Section 2 is numerically equivalent to the Green's Function-based technique derived by Montroll and Potts in [7] for large unit cells. In [7], Montroll and Potts model a single defect in an

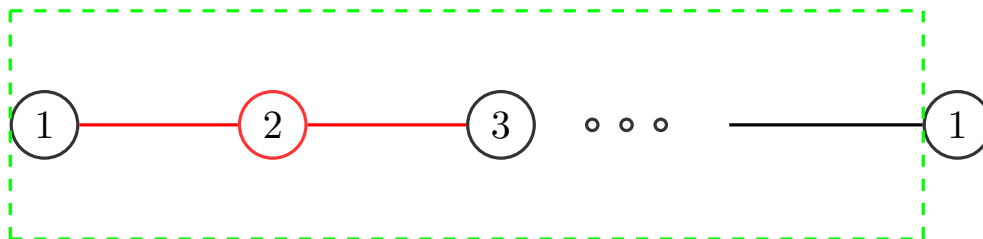


Figure 3.1: The one dimensional unit cell with $N \geq 3$ independent nodes, is demarcated by the green dashed lines. A point defect is located in the position of node 2.

infinite chain, whereas the operator methodology must be applied to periodic systems, which contain regularly spaced defects. The ratio of defective to non-defective atoms can be lessened within the periodic system by increasing the size of the unit cell. Thus the convergence to the dilute limit of [7] is a function of the number of atoms in each unit cell.

Consider the periodic geometry shown inside the green dashed lines of Fig. 3.1, with $N \geq 3$ nodes per unit cell. In this section I will calculate the rates of convergence of mode frequencies for a single defect in a periodic system to the infinite chain limit as a function of the unit cell parameter N . Unless otherwise indicated, interactions are assumed to have the same interaction potential as the pristine lattice. Note that ϕ and q used presently are identical to γ and P , respectively, in [7].

For $N = 3$, the pristine dynamical matrix can be calculated using (2.32) as

$$\mathbf{D}_p = \phi \begin{bmatrix} 2 & -1 & -e^{-i(\mathbf{G}\cdot\mathbf{a})} \\ -1 & 2 & -1 \\ -e^{i(\mathbf{G}\cdot\mathbf{a})} & -1 & 2 \end{bmatrix} \quad (3.1)$$

and assuming that all nodes have the same mass ($m_k = m, \forall k$), the pristine mass matrix from (2.26) is

$$\mathbf{M}_p = \begin{bmatrix} m & 0 & 0 \\ 0 & m & 0 \\ 0 & 0 & m \end{bmatrix} \quad (3.2)$$

A point defect can be created by altering a nodal mass and/or changing the strength

of the two nearest neighbor interactions of a node. Since the defective atom is located in the node 2 position, the mass of that node is set to $\mu_2 = \mu$, and $\mu_k = m$ for all other nodes $k \neq 2$. The mass matrix operator (2.12) is then

$$\mathbf{B} = \begin{bmatrix} 1 & 0 & 0 \\ 0 & \mu/m & 0 \\ 0 & 0 & 1 \end{bmatrix} \quad (3.3)$$

In this configuration, two interactions have modified force constants due to the point defect. The two damage coefficients associated with these interactions are q_{12}^0 (the damage factor corresponding to the bond between the first and second nodes) and q_{23}^0 (the damage factor corresponding to the bond between the second and third nodes in the reference unit cell). I will assume that the two linear damage coefficients are equivalent, $q_{12}^0 = q_{23}^0 = q$, and all other $q_{kk'}^0 = 1$. Using (2.42) and (2.9) in (2.5), the corresponding defect operator is

$$\mathbf{A}_{12}^0 = \mathbf{I} - \frac{q-1}{e-1} \begin{bmatrix} -e & -1 & -1 \\ e & 1 & 1 \\ 0 & 0 & 0 \end{bmatrix} \quad (3.4)$$

where $e = e^{i\mathbf{G}\cdot\mathbf{a}}$

The second operator (\mathbf{A}_{23}^0) maps the interaction between the second and third nodes in the reference unit cell into a “defective” state, and can be calculated using

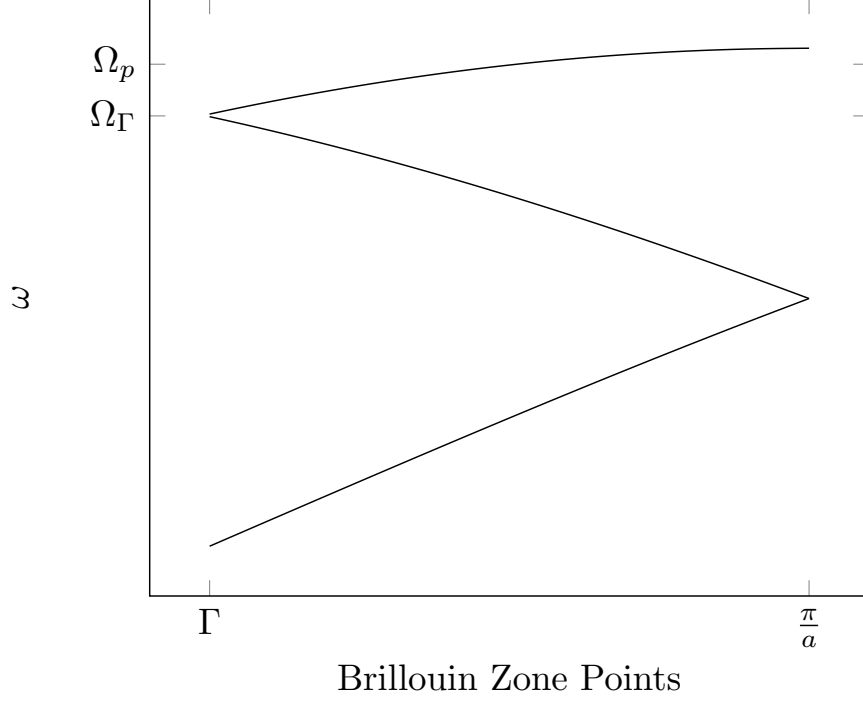


Figure 3.2: Dispersion curves for the pristine lattice between Γ , where $G = 0$, and $G = \pi/a$.

the same general procedure. The final defect operator \mathbf{A} is found to be

$$\mathbf{A} = \mathbf{I} - \frac{q-1}{e-1} \begin{bmatrix} -e & -1 & -1 \\ 0 & 1-e & 0 \\ e & e & 1 \end{bmatrix} \quad (3.5)$$

by substituting (3.4) and \mathbf{A}_{23}^0 into (2.18).

The pristine matrices in (3.1) and (3.2) can be substituted into (2.14) and subsequently used to determine the dispersion curves of the pristine lattice in the first Brillouin zone. These are shown in Fig. 3.2. If Ω_p is defined as the maximum frequency in the pristine lattice, the frequency ($\omega_p(G)$) in the pristine lattice can take continuous values between zero and Ω_p , with no band gap. Increasing the

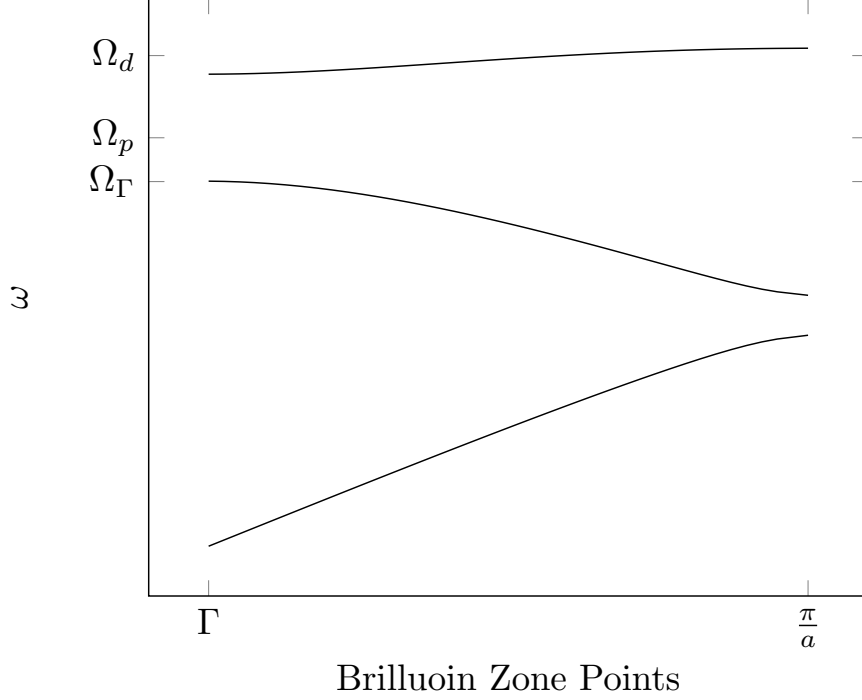


Figure 3.3: Dispersion curves for the defective lattice with mass ratio $\mu/m = 0.5$. For comparison, the maximum frequency of the pristine lattice Ω_p is shown.

number of nodes N in the unit cell increases the number of degrees of freedom, and therefore the number of continuous branches in the piecewise continuous dispersion curve through so-called zone-folding. However, regardless of the number of nodes in the unit cell, $\omega_p(G)$ ranges from zero to some finite maximum value Ω_p continuously with no frequency gaps.

The dispersion curves for a lattice containing a substitutional defect are shown in Fig. 3.3. This substitutional defect is simulated with an assumed mass ratio $\mu/m = 0.5$ of the defective node while the interaction potential remains unchanged from the pristine state ($q = 1$). The dispersion curves are determined using the pristine matrices (3.1) and (3.2) along with defect operators (3.5) and (3.3) substituted into (2.2). Any mass ratio less than 1 is found to produce a similar shift

in maximum frequency. As can be seen in Fig. 3.3, unlike the pristine lattice, the defective lattice contains band gaps. Furthermore, the highest frequency mode Ω_d in the defective lattice is higher than any of the available frequencies in the pristine lattice. In [7], Montroll and Potts refer to the modes in the defective lattice with frequencies higher than Ω_p as modes “whose frequencies are displaced out of the band.” The frequency labeled as Ω_Γ is the highest frequency mode at the Γ point, and is also the highest frequency mode unaffected by the defect parameter μ . In Fig. 3.3, the upward movement of Ω_d and the lack of change to Ω_Γ are consistent with the basic behaviors noted by [7].

Substitutional defects with values of the mass ratio less than one ($\mu/m < 1$), and no change in force constant induce localized modes, shifting the highest frequency mode to a higher value. Fig. 3.4 shows the ratio of Ω_d to Ω_p in systems with $N = 15, 5,$ and 3 nodes per unit cell where the mass of a single atom is parametrically changed. The solid line is the maximum frequency shift as a function of mass ratio in the infinite chain limit [7]. The shift in the maximum frequency (Ω_d/Ω_p) increases with decreasing defect mass ratio independent of the number of degrees of freedom. The present solution is numerically indistinguishable from the infinite chain or dilute limit solution of [7] for $N = 15$. The solid line in Fig. 3.6 shows that the convergence to the dilute limit goes as $\approx 1/N^{2.45}$; a very rapid convergence. It is expected that increasing the range of the interactions beyond nearest neighbors will result in a smaller convergence rate.

Vacancies can also generate localized modes. Following [7], a vacancy can be represented by a low mass ratio at the site of the vacancy ($\mu/m \approx 0.1$), and a high

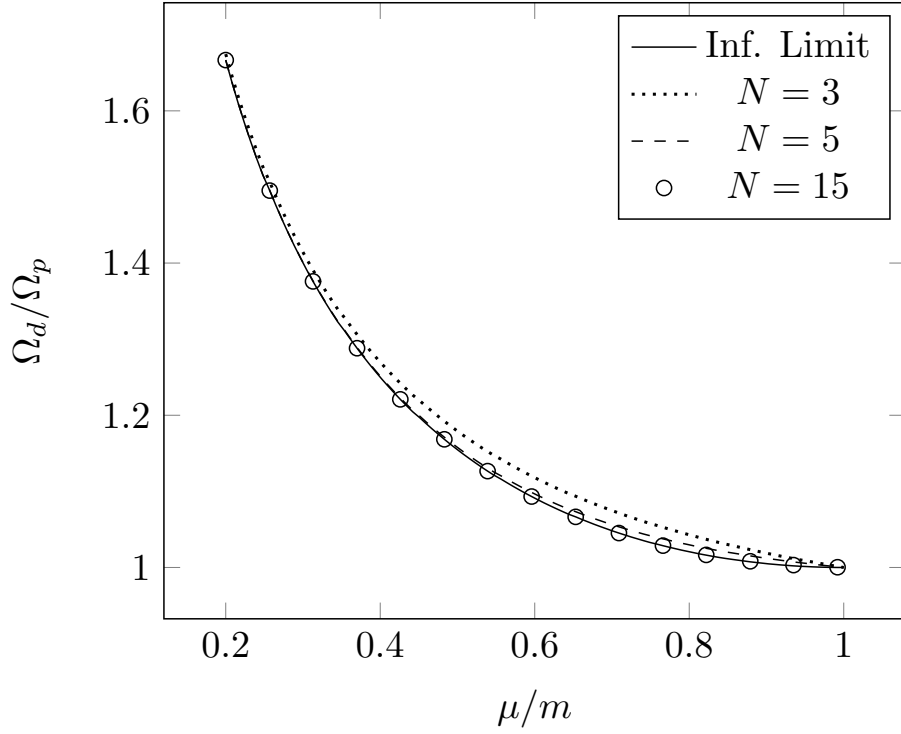


Figure 3.4: Shift of the maximum frequency as a function defective mass ratio compared to the results for the infinite limit calculates in [7].

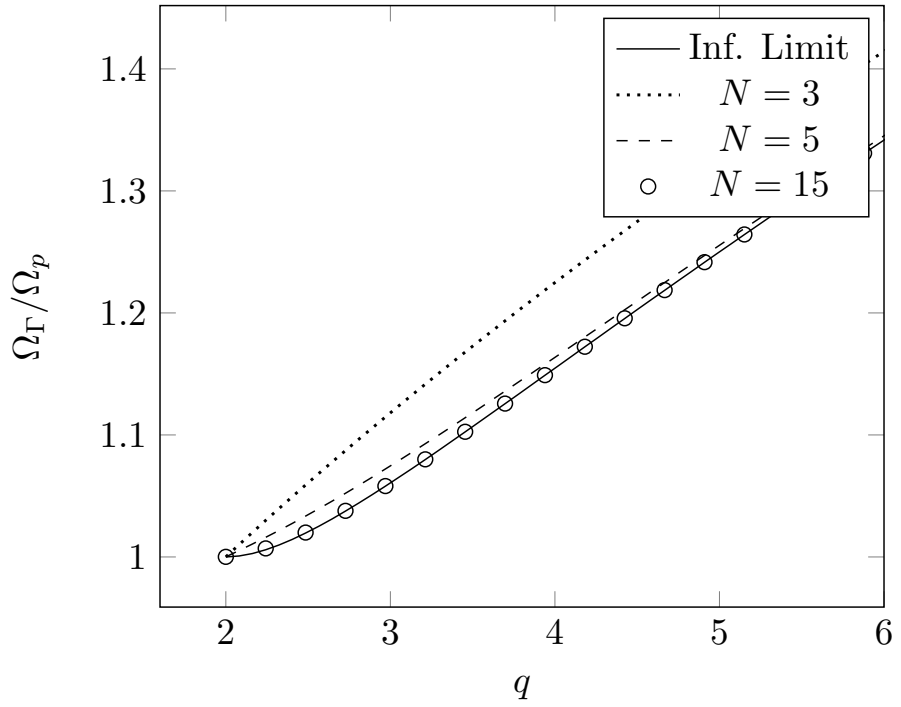


Figure 3.5: Frequency shift of Ω_Γ as a function of damage coefficient q compared to the results for the infinite limit calculates in [7]

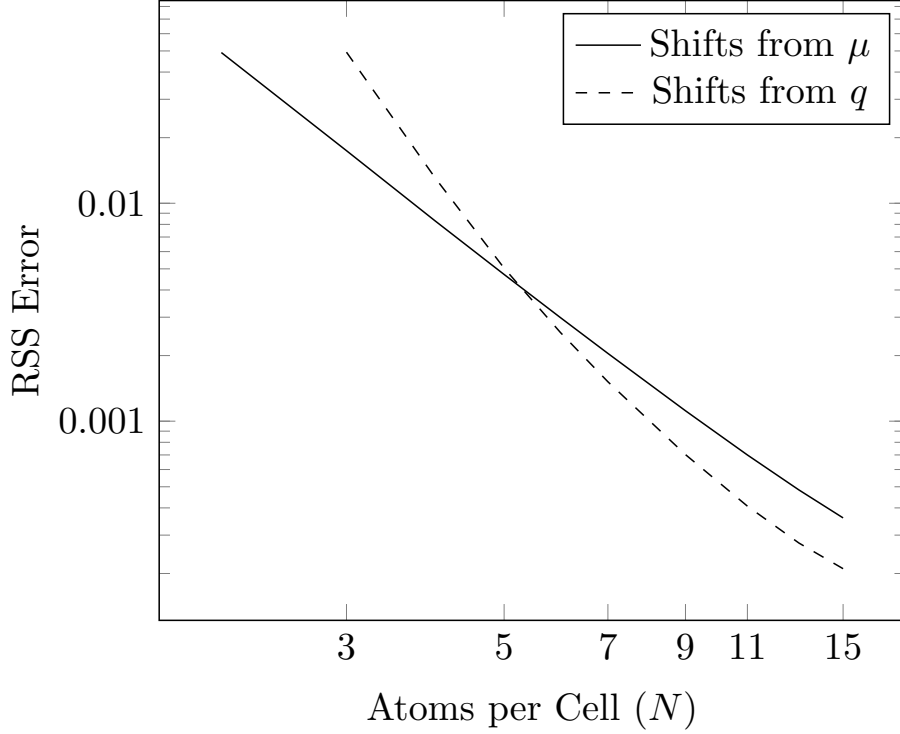


Figure 3.6: RSS error compared to the infinite limit as a function of the number of atoms per unit cell.

interaction potential between the vacancy and the neighboring atoms ($q \geq 2$) to account for relaxation. Fig. 3.5 depicts the effect of the parameter q on Ω_Γ , the highest frequency at the Γ point. In the dispersion curves for the pristine lattice, Fig. 3.2, $\Omega_\Gamma < \Omega_p$ and thus $\Omega_\Gamma/\Omega_p < 1$ for $q = 1$. In Fig. 3.5 it is shown that regardless of unit cell size, a value of $q = 2$ results in $\Omega_\Gamma/\Omega_p = 1$, and larger values of the damage factor q induce shifts in Ω_Γ higher than the maximum frequency of the pristine lattice. Once again the present results are numerically equivalent to the infinite chain solution of [7] for $N = 15$ atoms per unit cell. Using the best fit to the dashed line in Fig. 3.6, the rate of convergence is determined numerically and found to be proportional to $1/N^{3.35}$. Comparing this rate of convergence with that of the mass defect, it is interesting that the image interactions associated with an

altered interatomic potential decays more rapidly than the image interactions due to a substituted mass.

For each type of point defect, defective mass or defective potential, we see that a unit cell of $N = 15$ atoms is sufficient to compute the defect-induced frequency shifts of a dilute system. In systems with farther-reached bonds than nearest-neighbor, it is expected that a larger number of atoms would be required to isolate the effects of a single defect.

3.2 2D Rectangular Lattices with Central Forces

In this section applications are shown of the developments in Section 2 to problems representative of those encountered in the fields of molecular and structural dynamics. Two-dimensional systems are examined whose simplicity allows the complete matrix expressions to be shown. After first describing the example set-up in Section 3.2.1, two different defect types are studied: an atomic point defect in Section 3.2.2, and a structural defect in a truss structure using consistent (truss element) mass matrices in Section 3.2.3. The same pristine geometry, depicted in Fig. 3.7a, will be used for the examples. To use Eq. (2.5), one would generally determine the inverse of the pristine dynamical matrices $\mathbf{D}_p^{(1)}$ and $\mathbf{D}_p^{(2)}$ once and use the inverse as needed to find the defective spectra for any defect combinations of interest.

3.2.1 Example Set-up

In this section, pristine dynamical matrices are calculated for later use in Sections 3.2.2 and 3.2.3. Additionally, I will demonstrate the use of the equations in Section 2.2.2.2 for calculating the defect operators of a two-dimensional rectangular lattice with central forces. The unit cell contains four nodes for a total of eight displacement degrees of freedom. Both first and second neighbor interactions are used in these examples. In the two dimensional, rectangular cell, each node has four nearest neighbors and four next-nearest neighbors.

For the sake of simplicity, this example is limited to a monatomic crystal in which every node in the lattice is identical to all other nodes. The force constants for nearest neighbor interactions for a lattice at equilibrium are written as $\phi'_{kk'} = \phi^{(1)}$ and next-nearest neighbors as $\phi'_{kk'} = \phi^{(2)}$. The dynamical matrix contributions from nearest-neighbor interactions can be calculated using (2.38) and written,

$$\mathbf{D}_p^{(1)} = -\phi^{(1)} \begin{bmatrix} -2 & 0 & 1 + e_1^{-1} & 0 & 0 & 0 & 0 & 0 \\ & -2 & 0 & 0 & 0 & 1 + e_2^{-1} & 0 & 0 \\ & & -2 & 0 & 0 & 0 & 0 & 0 \\ & & & -2 & 0 & 0 & 0 & 1 + e_2^{-1} \\ & & & & -2 & 0 & 1 + e_1^{-1} & 0 \\ & & & & & -2 & 0 & 0 \\ & & & & & & -2 & 0 \\ & & & & & & & -2 \\ & & & & & & & & \textit{Hermitian} \\ & & & & & & & & & -2 \end{bmatrix} \quad (3.6)$$

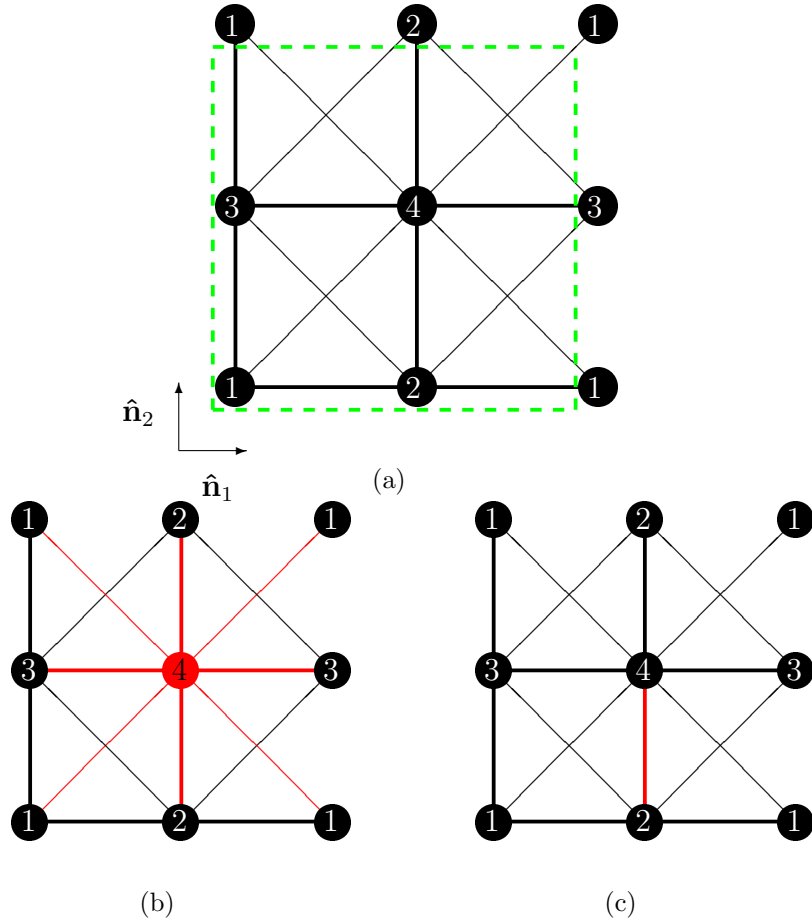


Figure 3.7: Two dimensional rectangular lattices with four independent nodes and nearest neighbor as well as next-nearest neighbor interactions. The length of each unit cell in the \hat{n}_1 direction is a_1 , and in the \hat{n}_2 direction is a_2 . (a) Pristine 2×2 unit cell. The green dashed lines indicate the periodic boundaries of the unit cell. (b) Point defect at node $k = 4$ with the eight affected interactions shown in red. (c) Defective structural truss in a rectangular lattice with the defective truss shown in red.

where the lower half the matrix is the complex conjugate of the upper half, and $e_1 = e^{i(\mathbf{G}\cdot\mathbf{a}_1)}$ and $e_2 = e^{i(\mathbf{G}\cdot\mathbf{a}_2)}$. The next-nearest neighbor dynamical matrix, $\mathbf{D}_p^{(2)}$, can be calculated in the same way.

In a monatomic system with $m_k = m\forall k$, the mass matrix of the pristine lattice \mathbf{M}_p using (2.26) is

$$\mathbf{M}_p = m\mathbf{I} \quad (3.7)$$

The defect operators are based on the interactions in the pristine lattice and can therefore be determined *a priori*. In Fig. 3.7a, consider the interaction between nodes 2 and 4 in the reference unit cell $l' = 0$, with the force constant $q_{24}^0\phi^{(1)}$. In what follows, the calculation proceeds by evaluating (2.42), determining the subsequent Δ terms with the help of (2.9), and multiplying by the inverse of the pristine dynamical matrix to get the defect operator \mathbf{A} of a single defective interaction using (2.8). Since the orthogonality condition (2.17) is satisfied for rectangular lattices, (2.18) may be employed.

From (2.42)

$$\mathbf{d}_{24}^0 = \phi^{(1)}(1 - q_{24}^0) \begin{bmatrix} 0 & 0 & 0 & 0 \\ 0 & 1 & 0 & -1 \\ 0 & 0 & 0 & 0 \\ 0 & -1 & 0 & 1 \end{bmatrix} \quad (3.8)$$

and substituting (3.8) into (2.9),

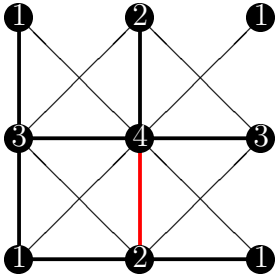
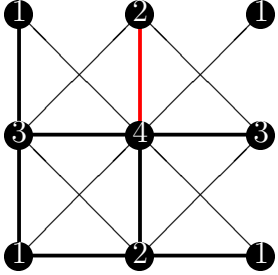
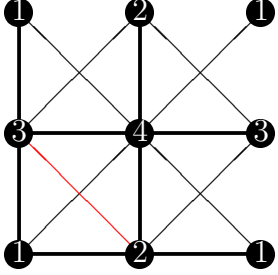
$$\Delta_{24}^0 = \phi^{(1)}(1 - q_{24}^0) \begin{bmatrix} 0 & 0 & 0 & 0 & 0 & 0 & 0 & 0 \\ 0 & 0 & 0 & 0 & 0 & 0 & 0 & 0 \\ 0 & 0 & 0 & 0 & 0 & 0 & 0 & 0 \\ 0 & 0 & 0 & 1 & 0 & 0 & 0 & -1 \\ 0 & 0 & 0 & 0 & 0 & 0 & 0 & 0 \\ 0 & 0 & 0 & 0 & 0 & 0 & 0 & 0 \\ 0 & 0 & 0 & 0 & 0 & 0 & 0 & 0 \\ 0 & 0 & 0 & -1 & 0 & 0 & 0 & 1 \end{bmatrix} \quad (3.9)$$

\mathbf{A}_{24}^0 may be determined from substituting (3.9) into (2.8)

$$\mathbf{A}_{24}^0 = \begin{bmatrix} 1 & 0 & 0 & 0 & 0 & 0 & 0 & 0 \\ 0 & 1 & 0 & 0 & 0 & 0 & 0 & 0 \\ 0 & 0 & 1 & 0 & 0 & 0 & 0 & 0 \\ 0 & 0 & 0 & \frac{e_2 q_{24}^0 - 1}{e_2 - 1} & 0 & 0 & 0 & \frac{q_{24}^0 - 1}{e_2 - 1} \\ 0 & 0 & 0 & 0 & 1 & 0 & 0 & 0 \\ 0 & 0 & 0 & 0 & 0 & 1 & 0 & 0 \\ 0 & 0 & 0 & 0 & 0 & 0 & 1 & 0 \\ 0 & 0 & 0 & \frac{e_2(1 - q_{24}^0)}{e_2 - 1} & 0 & 0 & 0 & \frac{e_2 - q_{24}^0}{e_2 - 1} \end{bmatrix} \quad (3.10)$$

This procedure follows the general methodology for calculating a defect operator, and may be repeated for each defective interaction. The operators are then used in Eq. (2.7) to obtain the defect dynamical matrix in Eq. (2.4). The $\alpha_{rr'}^{s'}$ are

Table 3.1: $\alpha_{rr'}^{s'}$ for three prototype interactions

| Interaction | α |
|---|---|
|  | $\alpha_{24}^0 = \frac{1-q}{1-e_2} \begin{bmatrix} 0 & 0 & 0 & 0 & 0 & 0 & 0 & 0 \\ 0 & 0 & 0 & -e_2 & 0 & 0 & 0 & -1 \\ 0 & 0 & 0 & 0 & 0 & 0 & 0 & 0 \\ 0 & 0 & 0 & e_2 & 0 & 0 & 0 & 1 \end{bmatrix}$ |
|  | $\alpha_{42}^1 = \frac{1-q}{1-e_2} \begin{bmatrix} 0 & 0 & 0 & 0 & 0 & 0 & 0 & 0 \\ 0 & 0 & 0 & 1 & 0 & 0 & 0 & 1 \\ 0 & 0 & 0 & 0 & 0 & 0 & 0 & 0 \\ 0 & 0 & 0 & -e_2 & 0 & 0 & 0 & -e_2 \end{bmatrix}$ |
|  | $\alpha_{23}^0 = \frac{1-q}{2(e_1-e_2)} \begin{bmatrix} 0 & 0 & -e_2 & e_2 & -e_1 & e_1 & 0 & 0 \\ 0 & 0 & e_2 & -e_2 & e_1 & -e_1 & 0 & 0 \\ 0 & 0 & e_2 & -e_2 & e_1 & -e_1 & 0 & 0 \\ 0 & 0 & -e_2 & e_2 & -e_1 & e_1 & 0 & 0 \end{bmatrix}$ |

determined in Table 3.1 for three of the basic interactions in the square lattice of Fig. 3.7a.

3.2.2 Point Defect in Square Lattice

The proposed methodology is now used to determine the phonon properties for a vacancy in a two-dimensional square lattice. I arbitrarily choose the lattice parameter and force constants to resemble those of a silicon mono-crystal. The point defect is located at node 4 in the 2×2 unit cell shown in Fig. 3.7b, and it is assumed that the force constants of all defective bonds are scaled in Eq. (2.37) by the same factor ($q_{rr'}^{s'} = q$). Thus, to create the vacancy, the eight interactions shown involving node 4 are effectively removed by setting $q = 0$, and the mass of node 4 is removed by setting $\mu_4 = 0$. The nearest neighbor dynamical matrix and the mass matrix of the pristine lattice were determined in (3.6) and (3.7) respectively.

Each node in the rectangular system has four nearest neighbors and four next-nearest neighbors. Therefore, a total of 8 individual defect operators can be combined to simulate the point defect. The defect operator matrix for one exemplary bond between nodes 2 and 4 was obtained in Eq. (3.10). The same procedure may be followed to determine the remaining defect operators, and then the individual defect operators may be substituted into (2.18) to determine the system defect operator for nearest and next-nearest neighbor interactions. These are, respectively,

$$diag(\mathbf{A}^{(1)}) = [1 \ 1 \ 1 \ q \ q \ 1 \ q \ q] \quad (3.11)$$

$$diag(\mathbf{A}^{(2)}) = [q \ q \ 1 \ 1 \ 1 \ 1 \ q \ q] \quad (3.12)$$

Note that (3.11) and (3.12) each become the identity matrix when $q = 1$. The system mass operator using (2.12) is

$$diag(\mathbf{B}) = [1 \ 1 \ 1 \ 1 \ 1 \ 1 \ \frac{\mu}{m} \ \frac{\mu}{m}] \quad (3.13)$$

which similarly becomes the identity matrix when $\mu = m$.

Pristine matrices (3.6)-(3.7) and operators (3.11)-(3.13) can be substituted into (2.15) to solve for the system modes as a function of the wave-vector \mathbf{G} . It is important to note that when nodes are removed ($q = 0, \mu = 0$), \mathbf{B} is not invertible, and therefore a matrix condensation or Lagrange multiplier approach must be employed.

Now, consider a single vacancy in a square lattice where $a_1 = a_2 = a$. At the so-called Γ point, where $\mathbf{G} = \mathbf{0}$ and $e_1 = e_2 = 1$, and assuming that the interaction potential is inversely proportional to length ($\phi^{(1)} = \sqrt{2}\phi^{(2)}$) the phonon modes are

$$\omega = \frac{\phi^{(1)}}{m} \begin{pmatrix} 0 \\ 0 \\ 2 + \sqrt{2} + \sqrt{6 - 2\sqrt{2}} \\ 2 + \sqrt{2} + \sqrt{6 - 2\sqrt{2}} \\ 2 + \sqrt{2} - \sqrt{6 - 2\sqrt{2}} \\ 2 + \sqrt{2} - \sqrt{6 - 2\sqrt{2}} \end{pmatrix} \quad (3.14)$$

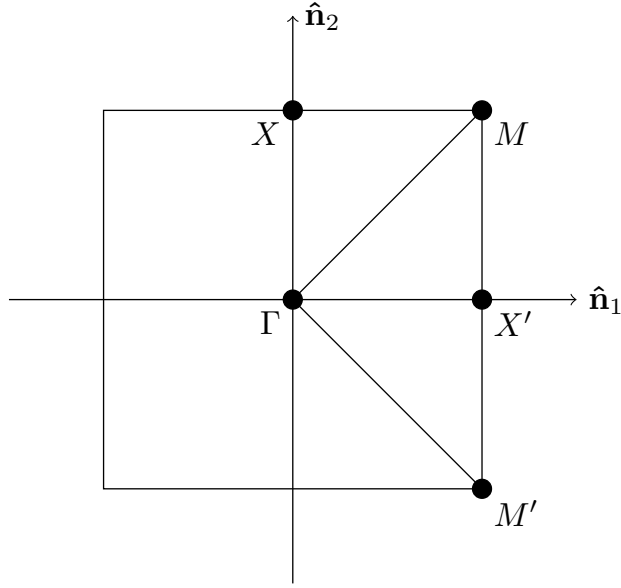


Figure 3.8: The first Brillouin zone and high symmetry points for the two-dimensional rectangular lattice. The boundaries of the Brillouin zone are located at $\pm\pi/a_1$ and $\pm\pi/a_2$.

The dispersion curves can be computed for any value of q or μ by solving for the system modes for the components of \mathbf{G} corresponding to points along the high symmetry lines. For this two-dimensional, square lattice, the first Brillouin zone is shown in Fig. 3.8. The corresponding density of states in the first Brillouin zone, are shown in Fig. 3.9 for damage factors of $q = 1$ and $q = 2$. The density of states plots were calculated using a direct count method [36]. A damage factor of $q = 1$ represents the pristine lattice. The damage factor of $q = 2$, could represent an alloy, dopant, or substitutional defect with an increased potential between the defective and non-defective atoms. As q is increased from 1 to 2, additional peaks appear in the density of states due to splittings of degeneracies. This is further shown in the dispersion curves in Figs. 3.10 and 3.11. At any point in the Brillouin zone the number of unique frequencies in the defective lattice is greater than or equal to the

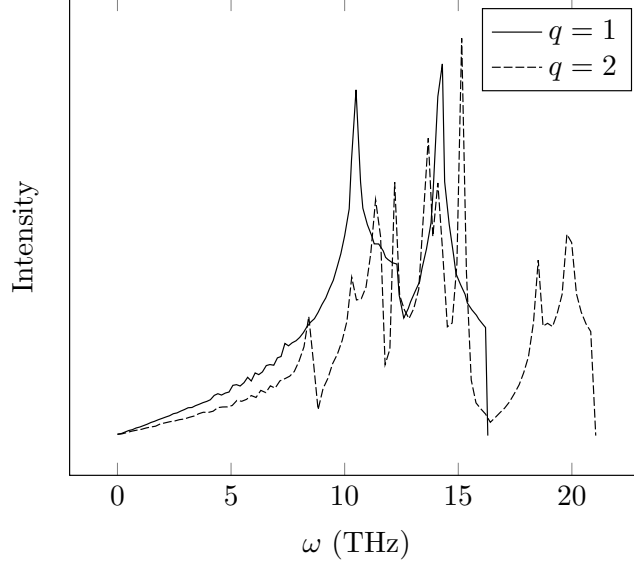


Figure 3.9: The density of states for the pristine lattice and a defective lattice. The parameters used to create the plots were $m = 5 \times 10^{-23}$ g, $\phi^{(1)} = .12$ eV/Å², and $\phi^{(2)} = .085$ eV/Å², and were chosen such that the range of frequencies was representative of silicon. The density of states for the pristine lattice ($q = 1$) is solid and the defective lattice with $q = 2$ is dashed

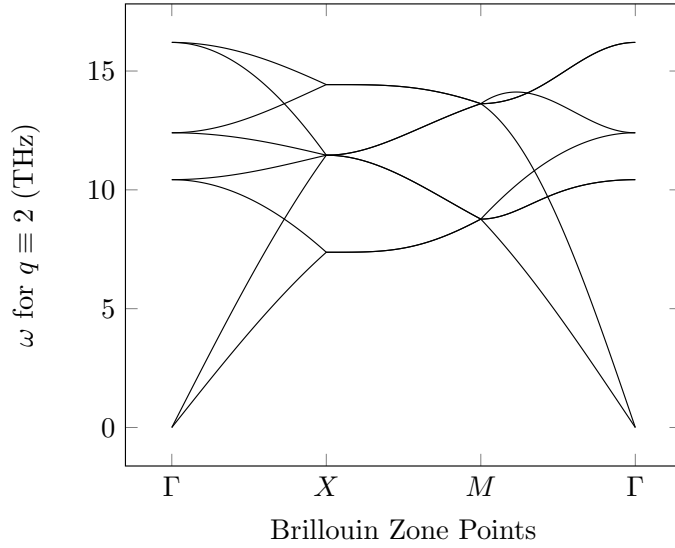


Figure 3.10: Dispersion curves of the pristine lattice using the same parameters as in 3.9.

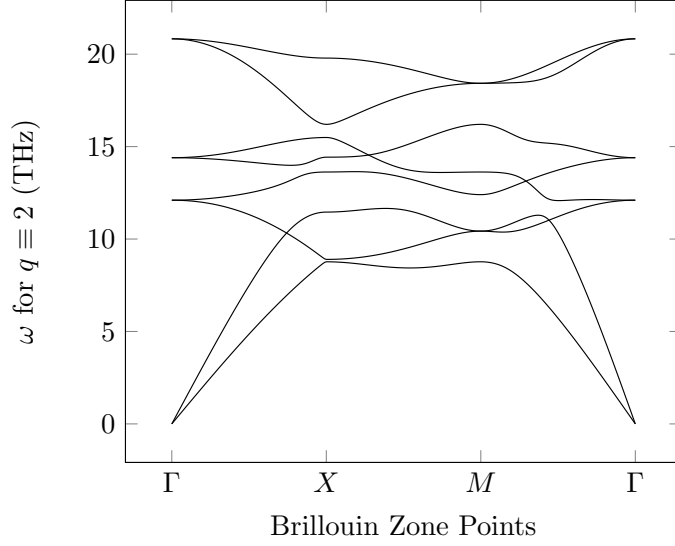
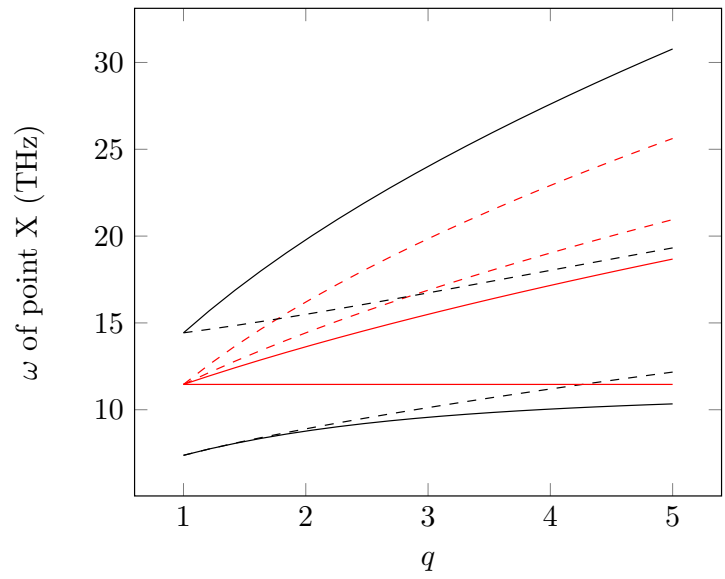


Figure 3.11: Dispersion curves of a point defect in a square lattice.

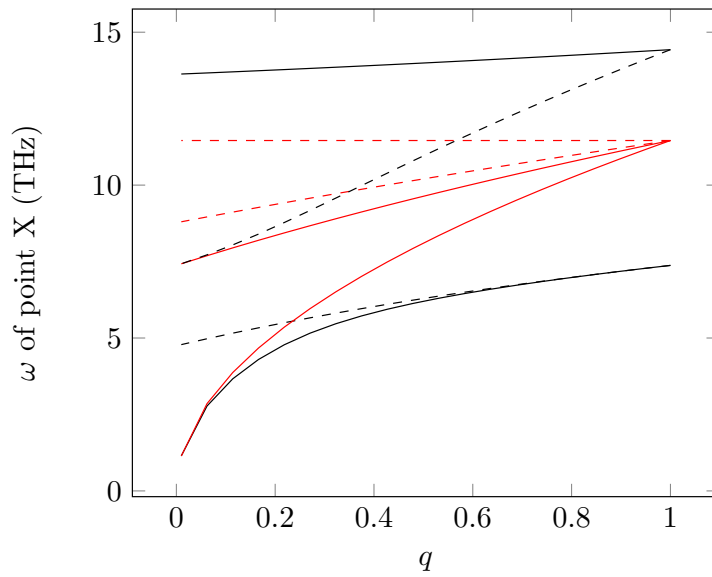
number of unique frequencies in the pristine lattice. For example, at the Brillouin zone point labeled as X , there exist exactly three unique frequencies in the pristine lattice, whereas in the lattice with a damage factor of $q = 2$, there exist 7 frequencies. The point defect has effectively caused modes to split, reducing the number of degenerate solutions. This is a consequence of the symmetry broken by the defects. In the pristine lattice, all four nodes are identical, and the lattice is symmetric under translations by integer multiples of $\mathbf{a}_1/2$ and $\mathbf{a}_2/2$. When the defect is introduced into the system, the lattice is only symmetric under translations by integer multiples of \mathbf{a}_1 and \mathbf{a}_2 . Additionally, while the pristine lattice is rotationally invariant to $\pi/2$ rotations about any node, the defective system is only rotationally invariant to $\pi/2$ rotations about node 4. Thus the defective system has fewer translational and rotational symmetries than the pristine lattice. This symmetry loss manifests in the splitting of degenerate phonon modes, and ultimately an increased number of peaks in the density of states plot.

A number of other changes can be observed in the resulting dispersion curves. Notice the two lowest energy modes at the X point, corresponding to transverse acoustic (TA) and transverse optical (TO) modes. In the pristine lattice, the TA and TO modes have the same energy levels given a wave-vector along the XM direction. However, in the defective lattice, the optical mode has a higher energy than the acoustic mode. Next, looking at the highest energy mode, the stiffened interactions in the defective lattice have induced a shift in this mode to an even higher frequency, effectively increasing the range of available frequencies in the lattice. Furthermore, at a damage factor of $q = 2$, the optical modes at the X point split, and begin to create an indirect band gap at approximately 16.2 THz bridged by the phonon modes at the M point. For values of $q > 2$, a full band gap is introduced into the system. Higher values of q would induce a wider band gap, and shift the system frequencies to even higher values.

In Fig. 3.12, the frequencies at point X are shown as a function of q . Point X was chosen to better study the band gap that appears in the $q = 2$ dispersion curve. As q increases to numbers greater than 1, the degenerate solutions split and shift farther apart, and the range of frequencies increases. Mode splitting, as in Fig. 3.12, manifests as an increased number of peaks in the density of states. Fig. 3.9 shows that the density of states curve for $q = 2$ has a larger number of peaks than for $q = 1$ and also a wider range of frequencies than the pristine lattice. This spread of frequency band, or the range of available frequencies in the density of states is in good agreement with the spreading of frequencies seen in Fig. 3.12a. The minimum available frequency is always zero for this lattice, regardless of q , however,



(a) $q \geq 1$



(b) $q \leq 1$

Figure 3.12: Mode frequencies at the high symmetry point X as a function of the damage factor q . In each figure, red and black lines indicate longitudinal and transverse modes, respectively. Similarly, solid and dashed lines indicate acoustic and optical modes, respectively. (a) Frequencies as q varies from 1.0 to 5.0. (b) Frequencies for $q < 1$.

the maximum available frequency increases with q . For some values of q , such as $q = 1.7$, new degenerate solutions form as the curves intersect, however, the number of unique modes for $q \neq 1$ is always greater than the number of unique modes at $q = 1$. As q increases past $q = 1.7$, the gap between the second and third highest dispersion curves at the X point is created, as seen in Fig. 3.11. Remarkably, longitudinal modes do not intersect other longitudinal modes, and transverse modes do not intersect other transverse modes except when the lattice is in the pristine state ($q = 1$).

In the limit as $q \rightarrow 0$, as depicted in Fig. 3.12b, the model is representative of a system with a vacancy. Recall that when node 4 is removed, two degrees of freedom are removed from the system, namely the displacement components of node 4 in the $\hat{\mathbf{n}}_1$ and $\hat{\mathbf{n}}_2$ directions. Therefore, two modes are expected to vanish as $q \rightarrow 0$, which is confirmed in Fig. 3.12b. These frequencies correspond to the two modes with the lowest frequency along the ΓX direction, a TA and an LA mode. The shapes of the TA mode are shown for three values of q in Fig. 3.13. In general, the shape of a mode is found by substituting the corresponding eigenvector into Eq. (2.19) at any time t . In these figures, time $t = 0$ has been arbitrarily chosen. As q decreases, the node 3 displacement goes to zero, and at $q \ll 1$, the displacement of all nodes except for node 4 are negligible. Thus at small values of q , node 4 oscillates in the $\hat{\mathbf{n}}_1$ direction. Similarly, in the LA mode (not shown), for small values of q , node 4 oscillates in the $\hat{\mathbf{n}}_2$ direction. At $q = 0$, node 4 is eliminated from the system, along with the LA and TA modes.

Changing the value of q does not change the number of modes (with the

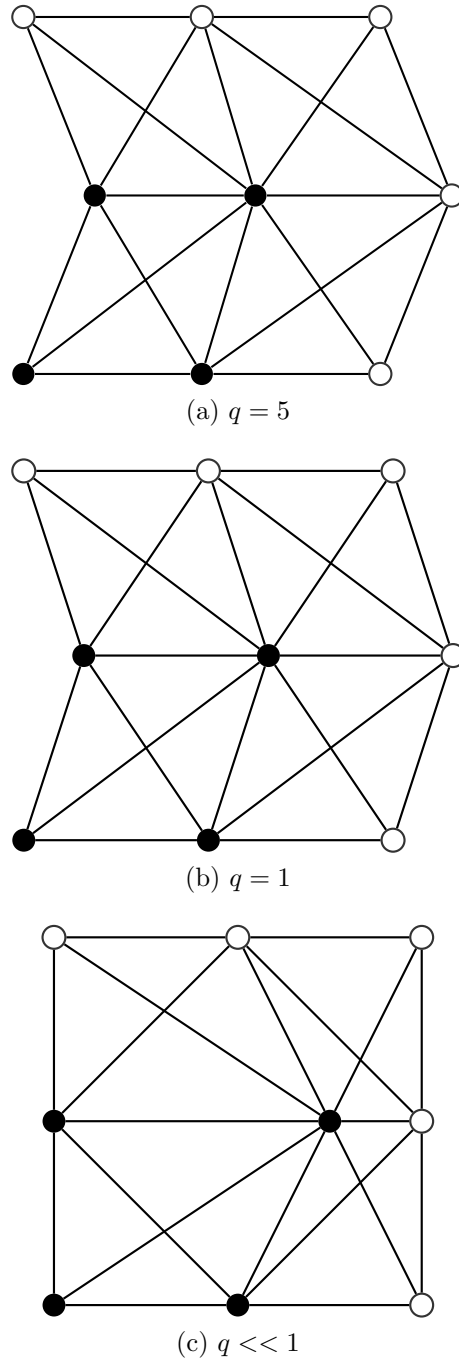


Figure 3.13: The shapes of the transverse acoustic mode at high symmetry point X for different values of q . The relative displacements are calculated by substituting the eigenvectors into equation (2.19) at time $t = 0$.

exception of $q = 0$) nor their longitudinal or transverse character. For $q > 0$, there exist exactly two of each of the mode classifications: LA, TA, longitudinal optical (LO), and transverse optical (TO), for a total of eight dispersion curves. Furthermore, for all values of $q > 0$, the lowest and highest modes at the X point are LA modes.

This atomic lattice example demonstrated the calculation procedure developed in Section 2 and provided potential insights into defect-induced mode splitting and shifting. In the next section, the same methodology is applied to an engineered structure with continuous mass between nodes.

3.2.3 Defect in Space Truss

This example examines a space truss structure that is comparable to the square lattice used in Section 3.2.2. Fig. 3.7c depicts the assumed geometry. I assume that a single truss member is damaged and examine the consequences on the vibration spectrum. In contrast to the previous example, a consistent mass matrix will now be employed based on a finite element discretization. Thus the two primary differences between this example and the example of 3.2.2 are the change in defect geometry and the use of massive interactions, or so-called bond masses [20].

The pristine dynamical matrices of this system are identical to those in Section 3.2.1 because the interaction geometry is the same. The pristine mass matrix, however, is now a consistent mass matrix. The consistent mass matrix $\mathbf{M} \in \mathbb{R}^{nN \times nN}$,

like the dynamical matrix is composed of $N \times N$ sub-matrices $\mathbf{M}_{kk'} \in \mathbb{R}^{n \times n}$

$$\mathbf{M} = \begin{bmatrix} \mathbf{M}_{11} & \mathbf{M}_{12} & \cdots & \mathbf{M}_{1N} \\ \mathbf{M}_{21} & \mathbf{M}_{22} & \cdots & \mathbf{M}_{2N} \\ \vdots & \vdots & \ddots & \vdots \\ \mathbf{M}_{N1} & \mathbf{M}_{N2} & \cdots & \mathbf{M}_{NN} \end{bmatrix} \quad (3.15)$$

If the mass of an interaction (i.e. a linkage or truss) between the k th node in the reference unit cell, and the k'' th node in the l'' th unit cell is $m_{kk''}^{l''}$, then each sub-matrix can be shown to be

$$\mathbf{M}_{kk'} = \sum_{k''l''} \frac{1}{6} m_{kk''}^{l''} \mathbf{v}_{kk''}^{l''} (2\delta_{kk'} + \delta_{k'l''}) \quad (3.16)$$

where the sum is taken over all nodes k'' in unit cells l'' that are connected to node k in the reference unit cell by a linkage or truss, and the mass of each linkage is

$$m_{kk''}^{l''} = \rho A |\mathbf{x}_{k''}^{l''} - \mathbf{x}_k^0| \quad (3.17)$$

where the mass density ρ and cross-sectional area A are assumed constant along the length and the same for all trusses. The defect operator can be derived using a similar method to the dynamical matrix defect operator. If $\mu_{rr'}^{s'} \in \mathbb{R}$ is the mass of the defective interaction, the resulting consistent mass defect operator analogous to (2.5) is

$$\mathbf{B} = \mathbf{I} - \sum_{r,r',s'} \Gamma_{rr'}^{s'} \mathbf{M}_p^{-1} \quad (3.18)$$

where $\mathbf{\Gamma}_{rr'}^{s'} \in \mathbb{R}^{nN \times nN}$ is a sparse matrix composed of a sub-matrix $\mathbf{g}_{rr'}^{s'} \in \mathbb{R}^{n \times n}$ just as $\mathbf{\Delta}_{rr'}^{s'}$ was shown to be composed of sub-matrix $\mathbf{d}_{rr'}^{s'}$ in Eq. (2.9). The sub-matrix $\mathbf{g}_{rr'}^{s'}$ is simply

$$\mathbf{g}_{rr'}^{s'} = \frac{1}{6}(m_{rr'}^{s'} - \mu_{rr'}^{s'}) \begin{bmatrix} 2\mathbf{v}_{rr'}^{s'} & \mathbf{v}_{rr'}^{s'} \\ \mathbf{v}_{rr'}^{s'} & 2\mathbf{v}_{rr'}^{s'} \end{bmatrix} \quad (3.19)$$

Assuming a square lattice with $a_1 = a_2 = a$, the length of all nearest neighbor and next-nearest neighbor interactions are $a/2$ and $a\sqrt{2}/2$, respectively, and the pristine mass matrix may be calculated from (3.16) as

$$\mathbf{M}_p = \frac{a\rho A}{12} \begin{bmatrix} 2 + 2\sqrt{2} & 0 & 1 & 0 & 0 & 0 & \sqrt{2} & 0 \\ & 2 + 2\sqrt{2} & 0 & 0 & 0 & 1 & 0 & \sqrt{2} \\ & & 2 + 2\sqrt{2} & 0 & \sqrt{2} & 0 & 0 & 0 \\ & & & 2 + 2\sqrt{2} & 0 & \sqrt{2} & 0 & 1 \\ & & & & 2 + 2\sqrt{2} & 0 & 1 & 0 \\ & & & & & 2 + 2\sqrt{2} & 0 & 0 \\ & & & & & & 2 + 2\sqrt{2} & 0 \\ & & & & & & & 2 + 2\sqrt{2} \\ \textit{Symmetric} & & & & & & & & 2 + 2\sqrt{2} \end{bmatrix} \quad (3.20)$$

The defect operator for the dynamical matrix is identical to (3.10). Since only a single interaction is damaged, using (2.18), $\mathbf{A} = \mathbf{A}_{24}^0$.

I introduce parameter $\epsilon \in \mathbb{R}$ to enable parametric study of the effect of different truss masses, where $\mu_{rr'}^{s'} = \epsilon m_{rr'}^{s'}$. The mass defect operator can be calculated from

(3.18) as

$$\mathbf{B} = \begin{bmatrix} 1 & 0 & 0 & 0 & 0 & 0 & 0 & 0 \\ 0 & 1 & 0 & 0 & 0 & 0 & 0 & 0 \\ 0 & 0 & 1 & 0 & 0 & 0 & 0 & 0 \\ 0 & .01(1 - \epsilon) & 0 & .42(\epsilon + 1.35) & 0 & .12(1 - \epsilon) & 0 & .12(\epsilon - 1) \\ 0 & 0 & 0 & 0 & 1 & 0 & 0 & 0 \\ 0 & 0 & 0 & 0 & 0 & 1 & 0 & 0 \\ 0 & 0 & 0 & 0 & 0 & 0 & 1 & 0 \\ 0 & .12(1 - \epsilon) & 0 & .12(\epsilon - 1) & 0 & .01(1 - \epsilon) & 0 & .42(\epsilon + 1.35) \end{bmatrix} \quad (3.21)$$

Once again, pristine matrices (3.6), and (3.20), and operators (3.10) and (3.21) can be used in Eq. (2.15) to determine the system modes. For comparison with the previous example, Fig. 3.14 depicts the density of states for the system in which bond strength is inversely proportional to length ($\phi^{(1)} = \sqrt{2}\phi^{(2)}$), with $\epsilon = 1$, and $q = 1$ or 2. In contrast to example 3.2.2, a consistent mass matrix has been used, and therefore qualitative differences exist between the plots in Figs. 3.9 and 3.15. Similar to the density of states in Fig. 3.9, the range of available frequencies expands once the defect is introduced into the system. One of the most apparent differences between the two curves in Fig. 3.14, is that the highest three peaks shift to even higher values when $q = 2$, and a new peak is formed at a frequency of $\omega = 1.2 \times 10^4$ Hz. These changes can most easily be seen in the dispersion curves, shown in Figs. 3.15a and 3.15b.

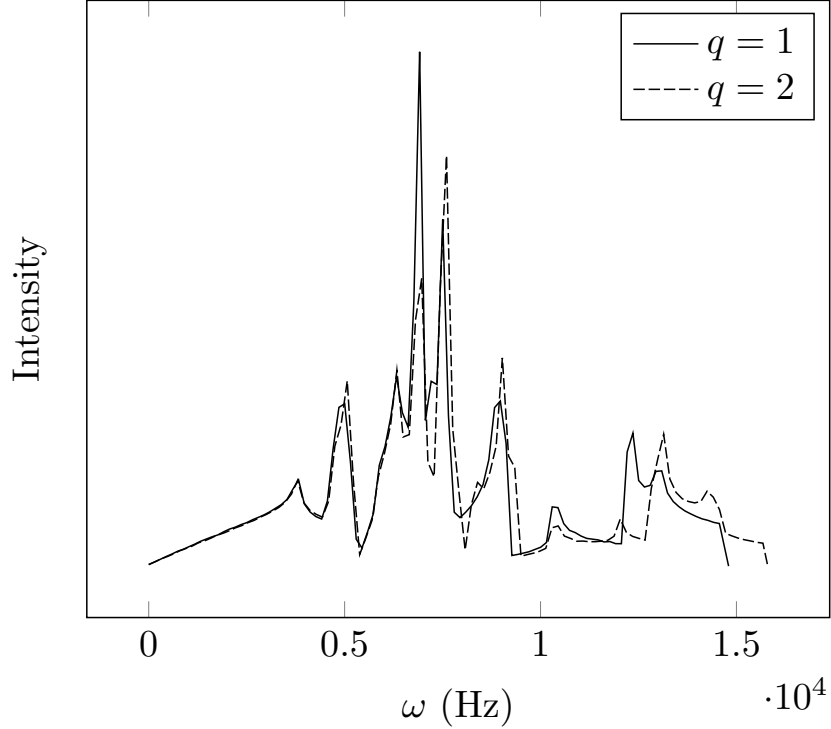
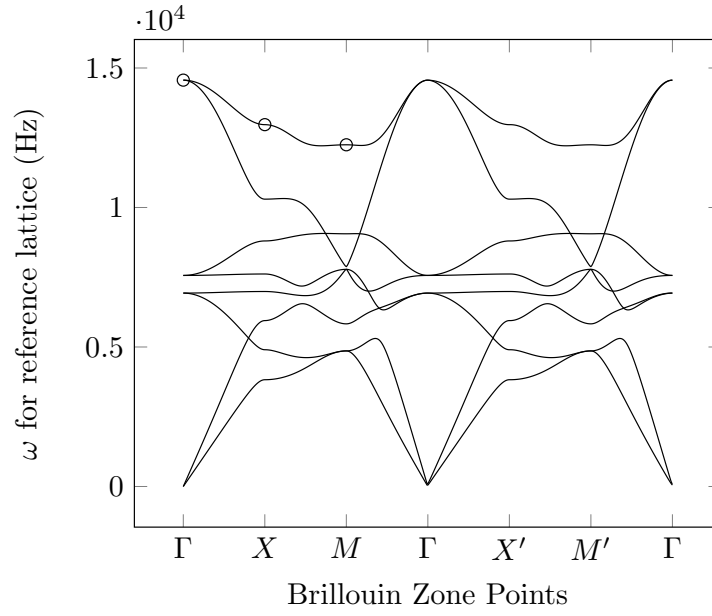
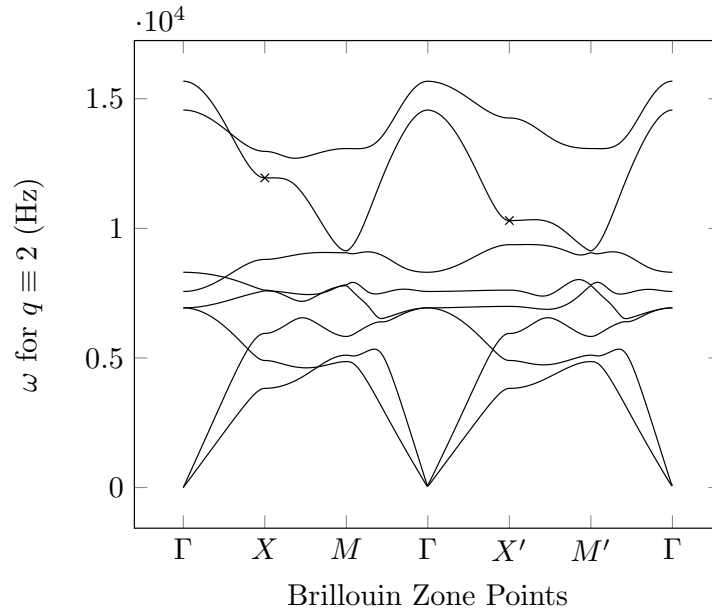


Figure 3.14: Density of states for two values of q . The parameters used to create the plot were $a = 2$ m, $\rho = 8000$ kg/m³, $A = 100$ cm², and $E = 200$ GPa. The density of states for the pristine lattice ($q = 1$) is solid and the defective lattice with $q = 2$ is dashed.

The highest three peaks in Fig. 3.14 correspond to the Γ , X , and M points along the highest frequency dispersion curve in Fig. 3.15a. The frequencies are circled in Figs. 3.14 and 3.15a for clarity. For the system with a defect parameter of $q = 2$, the frequencies corresponding to all three of these points on the dispersion curve are higher than the system with $q = 1$, which explains the blue shift in the highest three peaks. The new mode at $\omega = 1.2 \times 10^4$ Hz is related to the frequency values at the X and X' points along the second highest frequency dispersion curve, which are marked with the x symbol in Fig. 3.15b. In the pristine lattice, the frequencies are identical at the X and X' points. However, in the defective lattice this curve has different frequency values at the X and X' points. At the X point,



(a)



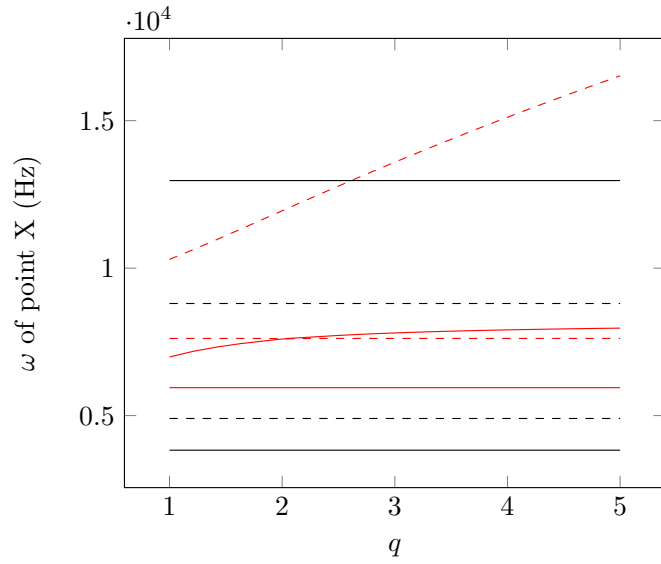
(b)

Figure 3.15: Dispersion curves for two values of q . The parameters used to create the plot were $a = 2$ m, $\rho = 8000$ kg/m³, $A = 100$ cm², and $E = 200$ GPa. (a) Dispersion curves associated with the pristine geometry. (b) Dispersion curves of the defective geometry.

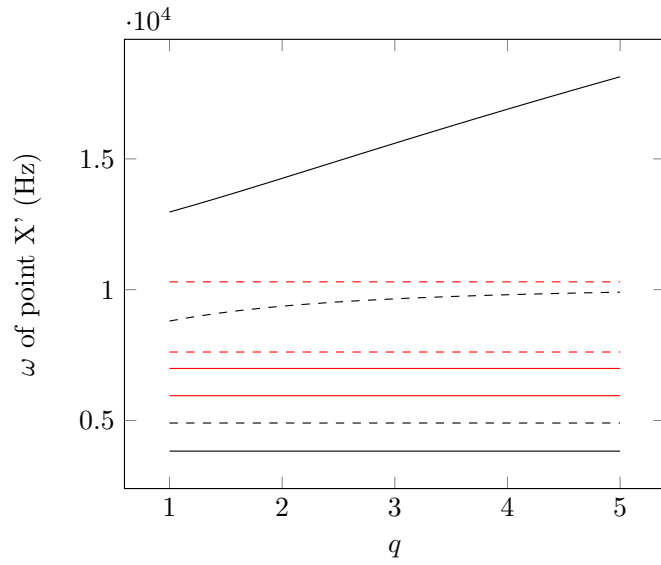
the frequency value is 1.2×10^4 Hz whereas the frequency at the X' point remains unchanged from the pristine lattice with a value of 1.0×10^4 Hz.

In fact, a general reduction in degeneracy at the high symmetry points located on the boundary of the first Brillouin zone can be observed. For example, Figs. 3.15a and 3.15b show that the third and fourth highest modes split at the Γ point, decreasing the number of modal degeneracies, whereas in Section 3.2.2, the modes shifted but did not split at the Γ point. This decrease in the number of degenerate solutions is due to the removal of the lattice rotational invariance. In the pristine lattice, the periodic truss is identical under $\pi/2$ rotations about node four, however, once a single truss is altered, this rotational symmetry is removed. In addition, the dispersion curves for the pristine lattice in the ΓX direction are identical to those in the $\Gamma X'$ direction, as can be seen in Fig. 3.15a. From Fig. 3.8, X corresponds to the point $\mathbf{G} = (0, \pi/a)$ and X' to $\mathbf{G} = (\pi/a, 0)$ such that the ΓX direction is a $\pi/2$ rotation from $\Gamma X'$. Similarly, the dispersion curves between X and M are identical to those between X' and M' in the pristine lattice, but this is not the case in the defective lattice.

The effects of the symmetry-reducing damage appear in the modes at high-symmetry points X and X' in Fig. 3.16. In a pristine lattice, the frequencies at these two symmetry points are identical due to rotational invariance. At each point, X and X' , exactly two modes shift when damage is introduced into the system, and all other modes remain constant. In Fig. 3.16a, these are indicated by the dashed and solid red lines with non-zero slope, and in Fig. 3.16b, they are indicated by the black solid and dashed lines. The two affected modes at the X point are

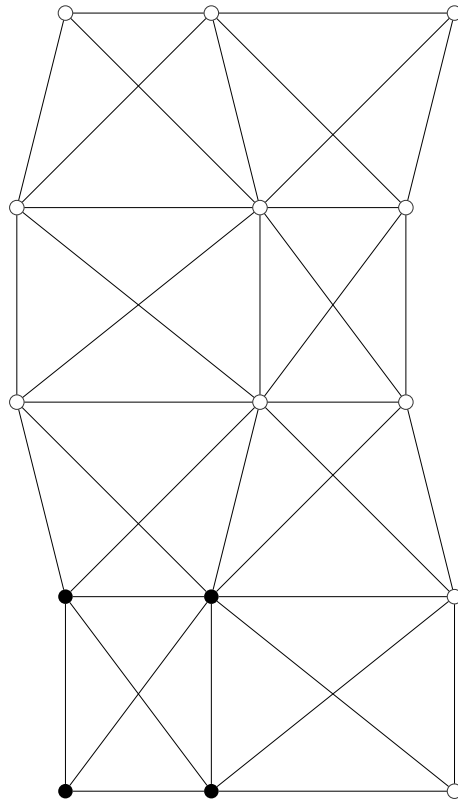


(a)

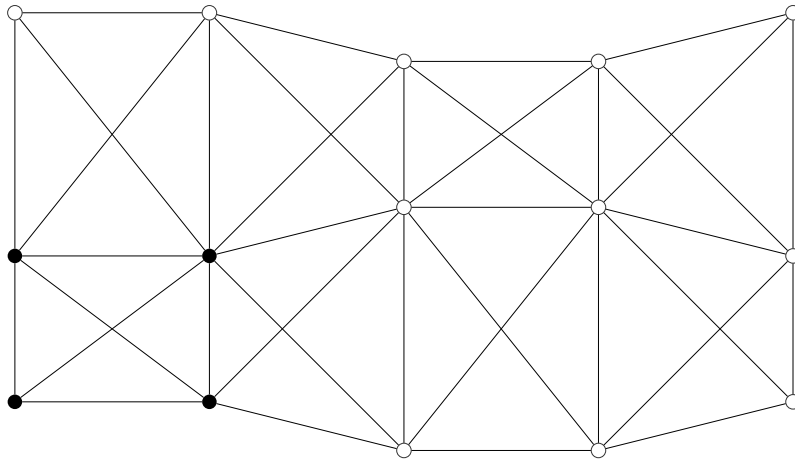


(b)

Figure 3.16: Mode changes at the high symmetry point X as a function of the damage factor q . In each figure, red and black lines indicate longitudinal and transverse modes, respectively. Similarly, solid and dashed lines indicate acoustic and optical modes, respectively. (a) Modes at point X for different values of q (b) Modes at point X' for different values of q .

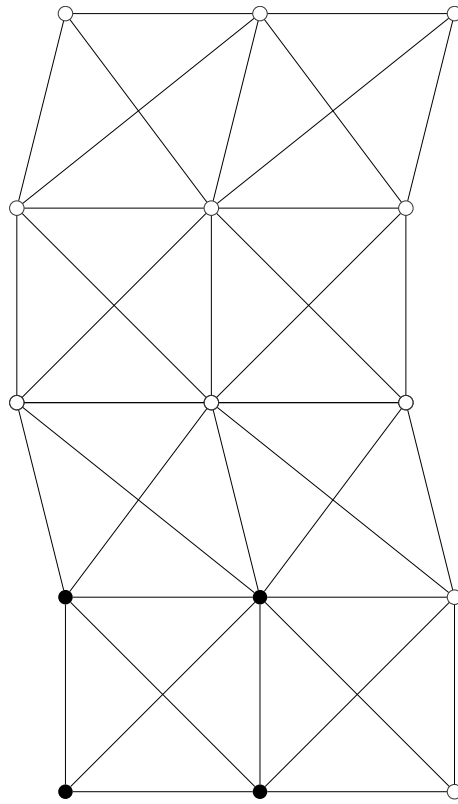


(a) Point X , $q = 1$

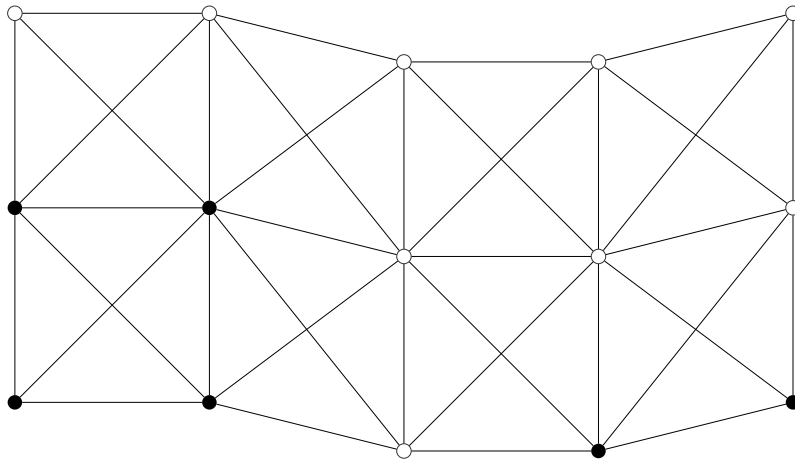


(b) Point X' , $q = 1$

Figure 3.17: The shapes of the highest frequency mode at point X and X' for damage factors of $q = 1$. The relative displacements are calculated by substituting the eigenvectors into Eq. (2.19) at time $t = 0$. A full period of the wave is shown in each image.



(a) Point X , $q = 1$



(b) Point X' , $q = 1$

Figure 3.18: The shapes of the lower energy transverse acoustic mode at point X and X' for damage factors of $q = 1$.

longitudinal modes, and at the X' point are transverse modes. This is expected because the damaged truss is oriented in the $\hat{\mathbf{n}}_2$ direction, and the wave-vectors at the X and X' points are oriented in the $\hat{\mathbf{n}}_2$ and $\hat{\mathbf{n}}_1$ directions, respectively. Thus, longitudinal modes at the X point, but transverse modes at the X' point can alter the length of the defective truss. As an example, the highest energy mode for the undamaged system is a transverse acoustic mode, depicted by the higher black solid line in both Figs. 3.16a and 3.16b. As q increases, the highest energy mode is unaffected at point X , but at point X' the frequency increases with q . The reason for this discrepancy can most clearly be seen by examining the shapes of the mode at each of the two points. The shapes of the highest frequency mode at points X and X' are shown in Fig. 3.17. At point X the length of the defective truss is unchanged during oscillations, whereas at point X' , the defective truss oscillates in length. Therefore, the damage parameter q has no effect on this particular mode at point X , but has a significant effect on both the mode shape and the frequency value at point X' . As with example 3.2.2, there exist exactly two of each mode type: TA, LA, TO, and LO. Remarkably, only the higher energy mode of each type is affected by damage at the X and X' points. Fig. 3.17b depicts the mode shape of the higher energy TA mode at the X' point. This mode can be compared with Fig. 3.18b, which shows the shape of the lower energy TA mode at the same point. Unlike the higher energy mode, the length of the defective truss is unchanged for the lower energy mode, and therefore, the value of q does not affect the frequency of the mode.

Similar plots can be shown for the LA, TO, and LO modes at the X and

X' points. For each type, the lower energy mode does not stretch or compress the length of the defective truss. The discrepancies between points X and X' and M and M' can also be viewed as mode splitting, or the splitting of degenerate solutions, which contribute to an increased number of peaks in the density of states.

3.3 Emulating Relaxation in a HCP Lattice with EAM Potential

In examples 3.2.2 and 3.2.3 the interaction potentials were modeled as linear with no compression or stretch, and the force between any given pair of nodes was zero, just as an unstretched spring transmits no force. Thus as interactions were altered or removed from the system, relaxation was not considered because the force profile and potential energy of the lattice remained unchanged. In this section, the empirical relations shown in Fig. 2.3 are used for Υ , Ψ and Φ of Eqs. (2.52) and (2.53). As mentioned in Section 2.2.3, these functions were developed in [34] to match experimentally measured properties of magnesium. Using the EAM potential, the forces between pairs of atoms are generally non-zero.

The force \mathbf{F} on a given atom k in unit cell l is calculated using (2.44) in (2.46) as

$$\mathbf{F}_k^l = \sum_{k''l''} \left(\left(\Upsilon'(\rho_{k''}^{l''}) + \Upsilon'(\rho_k^l) \right) \Psi'(r_{kk''}^{ll''}) + \Phi'(r_{kk''}^{ll''}) \right) \hat{\mathbf{n}}_{kk''}^{ll''} \quad (3.22)$$

and therefore the magnitude of the force between atom k in unit cell l and atom k' in unit cell l' is

$$F_{kk'}^{ll'} = \left(\left(\Upsilon'(\rho_{k'}^{l'}) + \Upsilon'(\rho_k^l) \right) \Psi'(r_{kk'}^{ll'}) + \Phi'(r_{kk'}^{ll'}) \right) \quad (3.23)$$

Using the values of Υ , Ψ and Φ from [34], the magnitude of the force between two nearest neighbor atoms in the magnesium lattice is 0.114 eV/Å. The non-zero force between atoms signifies that relaxation occurs in the presence of defects.

In the absence of relaxation, the operator method calculates the exact spectra for lattices containing point defects, as stated in Section 2. In this section I will first examine the effects of relaxation on the defective spectrum of magnesium in subsection 3.3.1. Then the methods of 2.2.3 will be utilized to emulate the phonon spectrum of a single vacancy in a relaxed magnesium lattice in subsection 3.3.2.

3.3.1 Relaxation in Magnesium

A sample unit cell for hexagonal-close-packed (HCP) magnesium is shown in Fig. 3.19. The red nodes indicate missing atoms due to a single vacancy. The pristine unit cell is therefore composed of the red and black solid nodes, while the unrelaxed system is composed of only the black nodes. The relaxed geometry was computed using the large-scale atomic/molecular massively parallel simulator (LAMMPS), and an exaggeration of this geometry is depicted by the gray nodes in Fig. 3.19. The trajectory of relaxation for each atom k in unit cell l may be computed using a relaxation factor of $\alpha = [0, 1]$ in the equation

$$\mathbf{x}_k^l = \mathbf{x}_{k_{unrelaxed}}^l + \alpha (\mathbf{x}_{k_{relaxed}}^l - \mathbf{x}_{k_{unrelaxed}}^l) \quad (3.24)$$

such that a relaxation factor $\alpha = 0$ represents a fully unrelaxed system, and a relaxation factor $\alpha = 1$ represents a fully relaxed system. Note that the nodes

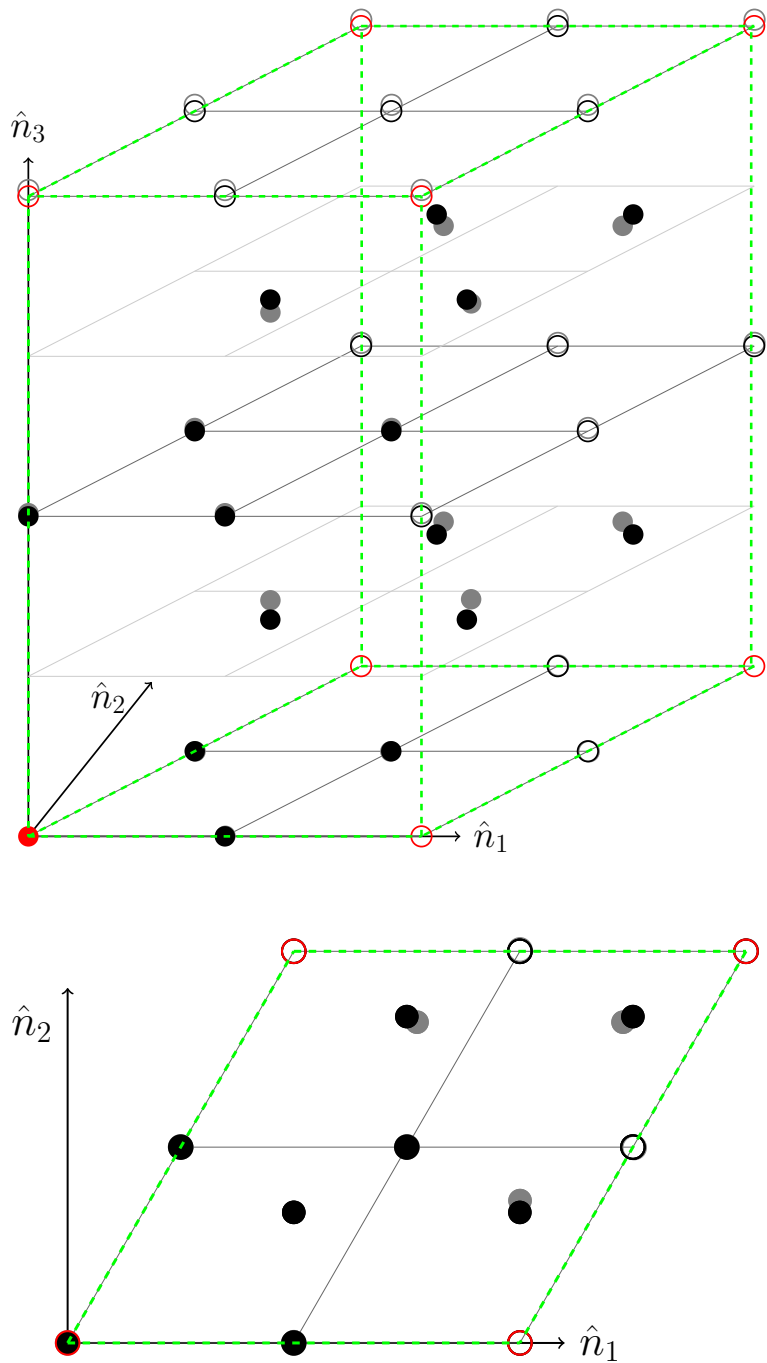


Figure 3.19: The unit cell for a hexagonal-close-packed lattice with a single vacancy and 16 unique atoms shown on the left. The nodes in the unrelaxed system are depicted by the black circles. The positions of the gray nodes are exaggerated from their true positions for the sake of increasing their visibility in this depiction. The top view is shown in the lower image.

on the second and third planes of the lattice travel farther away from the nearest vacancy site. This indicates that the vacant atom, when present, has an attractive force on these nodes.

Fig. 3.19 displays a single vacancy in a 16 atom unit cell. This configuration will be referred to as a 2^3 unit cell, as the HCP primitive cell is tiled two times along each of the three lattice vectors. As in Section 3.1, the effects of the vacancy can be diluted by using a larger unit cell, say a 3^3 unit cell of 54 atoms. The dispersion curves for the pristine primitive cell were shown in Fig. 2.4 in Section 2.2.3. Since the 2^3 unit cell contains a total of 48 degrees of freedom leading to 48 dispersion curves, a plot of the dispersion curves is not shown. Instead, the density of states was calculated using a direct count method [36]. Equations (2.26), (2.52), and (2.53) were used in (2.1) to solve for the frequencies associated with 10,000 randomly chosen wave-vectors within the first Brillouin zone.

The density of states for the pristine system is shown as the dashed line in Fig. 3.20. The red curve represents the spectrum of the unrelaxed geometry and the purple curve shows the spectrum of the relaxed geometry. The density of states is also shown for $\alpha = 0.5$ in yellow. For all values of α , the defective system has a larger number of peaks in the density of states plot than the pristine system. This is largely due to the removal of certain system symmetries due to the point defect, as discussed in example 3.2.2. Another notable difference between the pristine and defective spectra is the increased intensity of frequency modes between 1.8 and 3.8 THz and the decreased intensity of frequency modes between 3.8 and 4.2 THz. This red shift of modal frequencies can be attributed to the energy change of the lattice once the

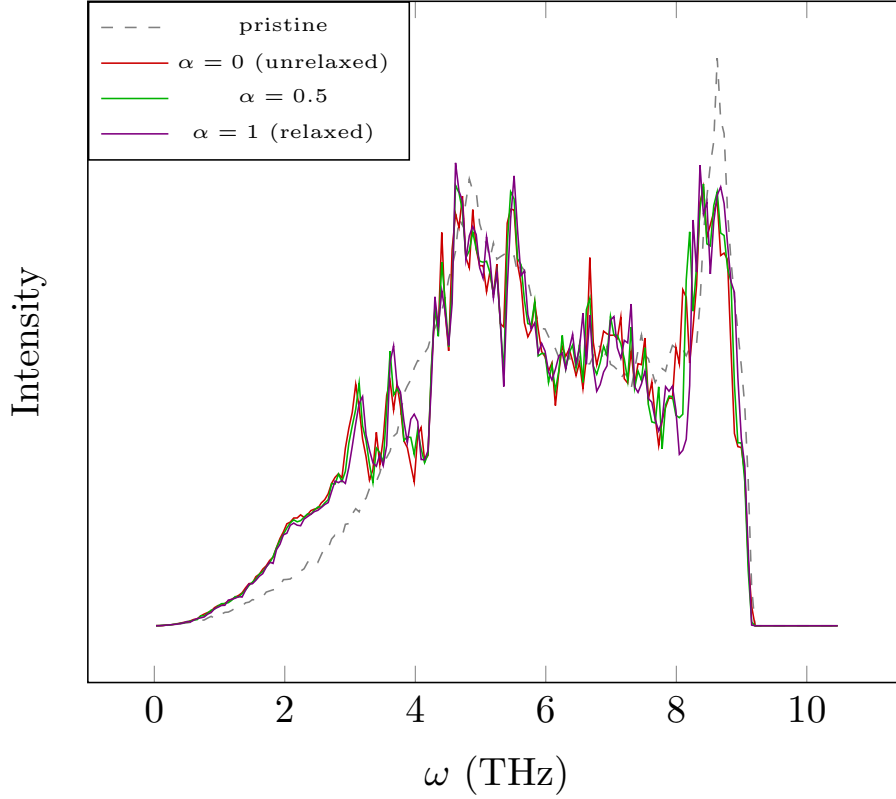


Figure 3.20: Density of states plots for magnesium using an EAM potential. The dashed line is the density of states of the pristine lattice. The solid lines represent the defective lattice geometry in various states of relaxation.

defect is introduced. The average energy per atom in each of the pristine, relaxed, and unrelaxed systems is -1.5287 , -1.4685 , and -1.4677 eV/atom, respectively. The magnitude of the energy per atom decreases for the defective systems, resulting in lower energy modes.

The shifts and splits of peaks within the density of states can be traced by varying the relaxation parameter α . For instance, the fully relaxed system has a peak at approximately 3.98 THz, whereas the fully unrelaxed system has a valley at the same frequency value. Observing the spectral peaks as α varies between 0 and 1, it appears that during the relaxation process a blue shift occurs for a mode

at 3.93 THz while a red shift occurs for a mode initially at 4.09 THz. These two frequency modes combine to form the peak in the relaxed system, signifying that a new degeneracy exists in the relaxed system which was not present in the unrelaxed system.

The unrelaxed spectrum may be exactly replicated using the operator method by setting $p = q = \mu = 0$ for the missing atom, and employing a Lagrange multiplier approach to eliminate three degrees of freedom. However, in Section 3.3.2 non-zero values of parameters p , q , and μ are explored to better approximate relaxation. This parameter-based relaxation is similar to that proposed in [7] and explored in Section 3.1 for a harmonic, one-dimensional chain. Montroll and Potts suggest values of $q > 1$ to approximate the shift of atoms towards a vacant atom site in [7]. In this system the neighboring atoms shift away from the vacant site, as seen in Fig. 3.19, and therefore values of $q < 1$ are expected to better simulate the relaxed geometry. In the next section, multiple values for q and p are explored to simulate the effects of relaxation.

3.3.2 Use of the Operator Method to Simulate Relaxation

Thermoelectric material properties are primarily functions of low frequency, acoustic phonon modes due to the relatively low group velocity associated with the high frequency, optical modes [37]. As such, the objective of this section is to determine the values of the parameters q , p , and μ that best reproduce the spectrum of the relaxed system for low frequency modes. I have chosen the cutoff frequency

of interest to be 5.2 THz, which is half of the maximum frequency of the magnesium lattice. I will define an error function as a measure of the distance between the relaxed spectrum and the spectrum computed using the defect parameters. This error is computed through

$$Error = \frac{\sqrt{\int_0^{5.2} (S_{def}(p, q, \mu) - S_{rel})^2 d\omega}}{\sqrt{\int_0^{5.2} (S_{pris} - S_{rel})^2 d\omega}} \quad (3.25)$$

where S_{def} is the spectrum computed using the defect parameters, S_{rel} is the spectrum of the relaxed lattice, and S_{pris} is the spectrum of the pristine lattice. The denominator of (3.25) is a constant value for all p , q , and μ , but is a function of defect density, geometry, and potential.

The process for determining the error associated with a set of parameters is as follows, first (2.56) and (2.57) are used in (2.52) and (2.53) to compute the defective dynamical matrices. Then the frequencies are computed at a random set of points within the first Brillouin zone using (2.14). The density of states is then calculated using a count method, and substituted into (3.25) to find the error. Parameters that produce errors less than 1.0 manipulate the pristine lattice into a state closer to the relaxed lattice, whereas parameters that produce errors greater than 1.0 manipulate the lattice into a state less like the relaxed system.

Surface plots of the error as functions of p and q are shown for four different values of μ in Fig. 3.21. As can be seen, all values of μ produce curves with steep decreases in error for $p \lesssim 3.5q$. In the pristine lattice, each atom has a value of $\rho = 4.09$, and $\Upsilon(\rho) = -3.3$ eV, which is well to the left of the minimum of $\Upsilon(\rho)$

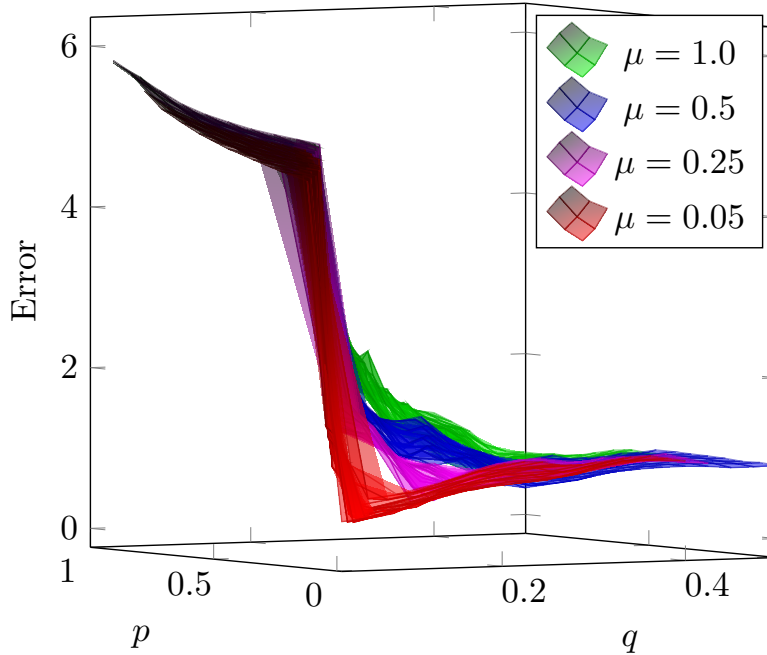
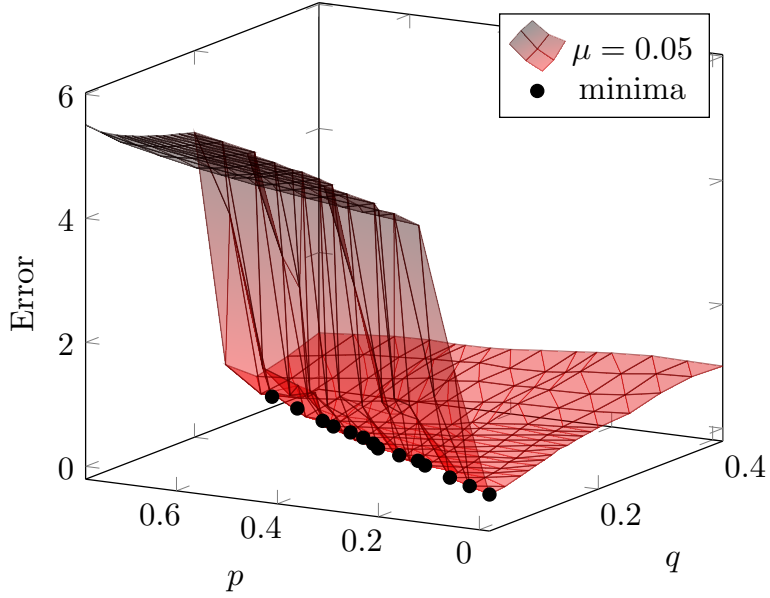
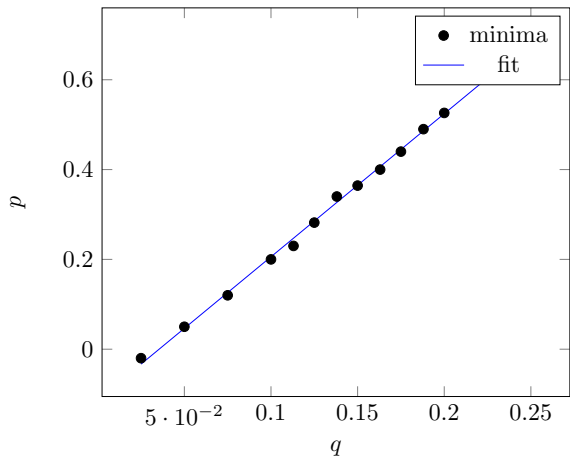


Figure 3.21: Error between the density of states of the relaxed geometry and the density of states using various defect parameters μ , p , and q in the 2^3 system.

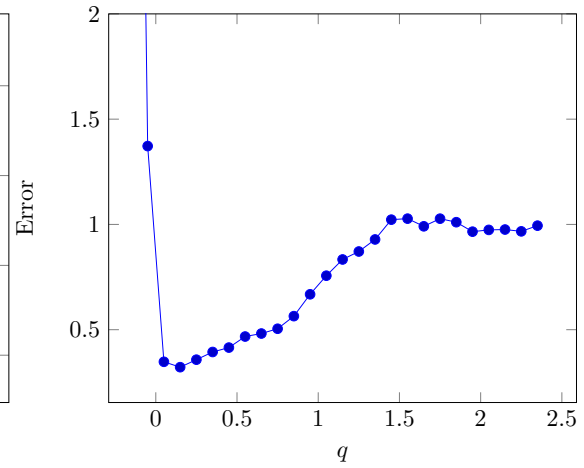
for magnesium, as seen in Fig. 2.3. Thus increasing p results in greater attraction between the vacant node and its surrounding neighbors. Conversely, increasing the value of q increases the repulsion between the vacant node and the surrounding neighbors. Since the neighboring atoms are repelled from the vacant node during relaxation, intuitively it follows that there should be an upper bound on p with respect to q to emulate the behavior of the vacancy. Notably, all four surfaces appear to converge around an error of 1.0 for parameters following $p \ll 3.5q$ regardless of the value of μ . Furthermore, low values of μ result in a smaller minimum error. This is expected because the vacant site in the relaxed lattice has no mass, and thus a low value of μ better matches the inertial properties of the defective lattice. Values of $\mu < 0.05$ were also considered, however, there was a negligible difference between the surface plots for $\mu = 0.05$ and lower values such as $\mu = 0.005$. As such, it was



(a)



(b)



(c)

Figure 3.22: Detailed error plots for a vacancy in 2^3 lattice with $\mu = 0.05$. (a) Error between the density of states of the relaxed geometry and the parameterized system are shown in red for $\mu = 0.05$. The circled points show local minima along the constant p and constant q lines. (b) Best fit curve for the local minima. (c) Error profile along the minimum line

assumed that the minimum error occurs along the surface of the $\mu = 0.05$ plot.

The following procedure was used to find the properties associated with the minimum error. First the minima along the lines of constant q on the surface plot for $\mu = 0.05$ were located. These data points are shown in black in Fig. 3.22a. Next, a line of best fit was calculated to approximate the locations of the point of minimum error, as shown in Fig. 3.22b. Incidentally, the equation of the line of best fit was found to be $p = 3.1864q - 0.1129$, and the residual squared value of the fit was $R^2 = 99.9\%$ [38]. Finally, the error profile traveling along this line of best fit was computed at regularly spaced intervals (Fig. 3.22c) and the minimum error was found to be 0.322, at $p = 0.37$ and $q = 0.15$. For comparison purposes, the values of $p = q = \mu = 0$ (the unrelaxed system) yields an error of 0.423. Therefore by this measure, the parameters yield a spectrum that is 24% closer to the relaxed spectrum than the unrelaxed spectrum.

The density of states for the minimum error solution is shown on top of the relaxed and pristine spectra in Fig. 3.23. Qualitatively, it appears that minimizing the error function (3.25) produced a defective spectrum similar to the relaxed system. For several applications including defect detection through Raman Spectroscopy, the frequencies associated with each peak in the density of state plot is perhaps the most critical value to simulate accurately. These peak frequencies are tabulated in 3.2 for the relaxed, minimum error, and unrelaxed systems. The first, second, fourth, fifth, and ninth peaks in the relaxed density of states are better represented using the minimum error solution than they are by the unrelaxed system. Only the seventh, tenth, and eleventh peaks are better approximated by the unrelaxed

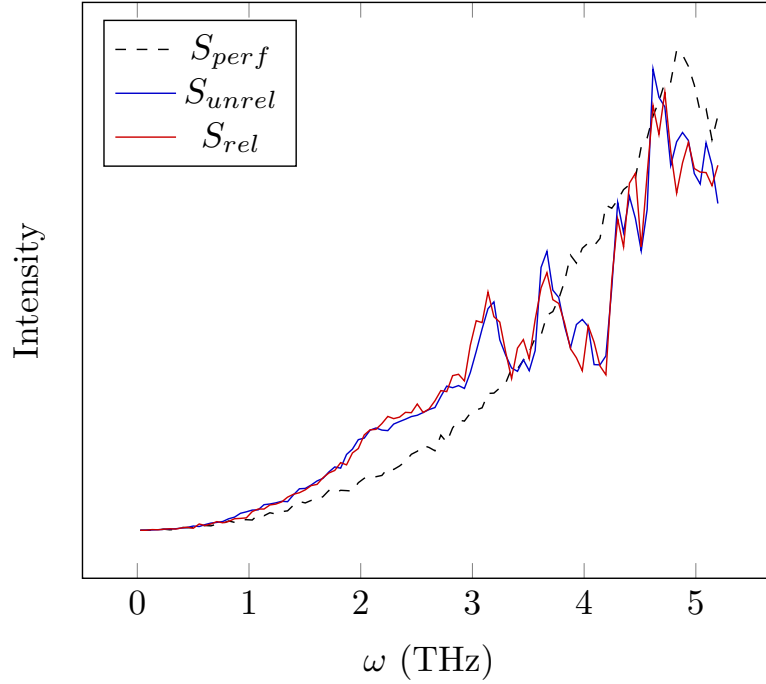


Figure 3.23: The density of states for the system with minimum error can be seen as the red solid line. Similarly, the density of states for the relaxed and pristine systems are the blue solid line, and black dashed line, respectively.

solution.

| Peak Num. | Relaxed | Min. Error | Unrelaxed |
|-----------|---------|------------|-----------|
| 1 | 3.1922 | 3.1394 | 3.0867 |
| 2 | 3.456 | 3.456 | 3.4033 |
| 3 | 3.6143 | | |
| 4 | 3.6671 | 3.6671 | 3.7198 |
| 5 | 3.9837 | 4.0364 | 4.0892 |
| 6 | 4.3003 | 4.3003 | 4.3003 |
| 7 | 4.4058 | 4.4585 | 4.4058 |
| 8 | 4.6168 | 4.6168 | 4.6168 |
| 9 | 4.7224 | 4.7224 | |
| 10 | 4.8807 | 4.9334 | 4.8807 |
| 11 | 5.0917 | | 5.1445 |

Table 3.2: Frequencies in THz associated with each peak in the lower half of the density of states curves. The values are tabulated for the relaxed, unrelaxed, and minimum error spectra.

Chapter 4: Conclusion

4.1 Contributions

This thesis derived a general methodology for modeling defects in periodic lattices across multiple length scales. Presently, when the accurate atomic structure of any defect is known, it is a simple matter to determine the dynamical matrix and its accompanying dynamic properties. Of interest in the present work is the ability to investigate variations in the structure-property relationships under variations of the defect structure and/or defect parameters. Such a capability could potentially enable parametric study and design of the vibration and phonon transport properties in lattice-based structures and materials. To this end, an approach for systematically composing the dynamical matrices of lattices containing defects is developed.

The developments are based on the proposition that the terms in the equations of motion, specifically the mass and dynamical matrices, can be transformed using a derived linear operator, and the operator is solely based on the pristine lattice configuration. That is, any lattice defect can be reduced to a set of basic transformations on the pristine lattice, where the transformations involve nodal masses or the direction and magnitude of the forces among nodes. Complex defects therefore are composed by any number of basic interactions through the use of defect

operators by applying those operators to the pristine lattice dynamical matrix. The entire framework is amenable to computer implementation and can scale to arbitrarily large unit cells. In contrast, established analytic methods require Greens functions, or numerical solutions must develop a separate dynamical matrix for every possible defect configuration in every possible unit cell of interest without direct relationships to the pristine host lattice.

A key result is in the formulation of an operator that can be composed of multiple matrices that either add or multiply together depending on the symmetry of the original pristine lattice. The multiple matrices contribute to create a system-level defect operator that, when multiplied to the original dynamical matrix of the pristine lattice, gives the exact dynamical matrix of the lattice containing this deliberate arrangement of defects in the absence of relaxation. Then, the solution to the associated eigenproblem can be obtained directly from the resulting expressions.

The present effort is exact only under the harmonic approximation in the absence of local relaxation around the defect core. In systems with relaxation, the operator method may be used to emulate the spectrum of the relaxed lattice with some finite error. The present results and analyses focus on the variations in vibration spectra as functions of defective potential and mass ratios. In one-dimensional lattices, the convergence to the infinite chain limit is numerically demonstrated. The dispersion properties of a periodic unit cell containing 15 nodes is numerically indistinguishable from the infinite chain solution. A finite defect density, through the indirect consideration of periodic image interactions, results in an increasing frequency shift when the mass of a point defect decreases or the local forces among

nodes increase.

For the sake of demonstrating the calculation approach using manageable matrix sizes, two-dimensional square lattices are studied using central force interaction potentials within the harmonic approximation. Varied defect structures are studied parametrically to investigate the parametric dependence of splitting and shifting of degeneracies as a function of the local nodal masses and forces. The calculated band structures of the vibration spectra reveal quantifiable parametric dependencies of band gaps and frequency maxima. The number of additional peaks in the density of states plot is found to correlate with the symmetry of the system in the two examples provided.

Finally, the methodology is applied to a three dimensional magnesium lattice with tabulated EAM potential functions. Relaxation within the non-linear lattice was simulated using the defect parameters. A 24% reduction in error in the density of states plot was demonstrated by using the operator method as compared to the unrelaxed geometry.

4.2 Future Work

This thesis focused first on the development of the operator method, and then on applications to atomic lattices with point defects as well as engineered structures with damaged members. In Section 3.3, the possibility of simulating relaxation using the proposed operator-based approach was assessed. As the scope of the research to date has primarily involved the derivation of a new methodology, there still remain

numerous applications for future study. The two primary areas of study on which I plan to focus are the design and detection of defects.

The design of phonon spectra has become a wide area of study, as discussed in Section 1.1.2. Already in Section 3.2.2, we derive defect properties that create a phononic band gap. For the simple, two-dimensional structure studied, it was shown that values of $q > 2$ of an atomic point defect produced a full band gap at approximately 16 THz. In the future, I wish to develop an approach for the design of acoustic band gaps at specified frequencies. For instance, using the operator method, perhaps one could design a system with a band gap covering a portion of the human auditory spectrum (approximately 20 Hz to 20 kHz [39]). Or perhaps a system could be designed to filter out high frequency noise from a recording device in an experimental setup. For these design applications, I plan to study systems that are periodic at the continuum-level with elastic potential functions between nodes, as in [12, 22–24, 40]. I choose to focus on continuum-level design and not atomic because the fabrication tools to build such devices are more readily available.

By detection, I am referring to the detection of the presence and possibly the location of defects or damage within a system. The applications in the field of defect detection could be at any level—atomic, continuum, or structural. However, I plan to focus my efforts on atomic defect detection. In this work, some of the ways in which the dispersion curves and density of states shift and split in the vicinity of a point defect were explored. First and foremost, I plan to study the effects of defect density on these predicted spectral shifts. The high defect densities explored in this work are not unlike the hydrogenated graphene of [2] or the silicon germanium of [4], and the

analysis performed herein could be useful in applications such as determining alloy material percentages from measured Raman spectra. However many applications require extremely low defect densities. Using the unit cell in Section 3.3, I plan to determine the rate at which the defective spectrum converges to the pristine spectrum as a function of unit cell size. This should provide a guideline for the defect densities that could realistically be detected within the bulk of a material. There might be, however, an opportunity to detect low densities of defects using the localized modes created around each defect. Localized modes, which are functions of anharmonicity and are therefore not calculable using the operator method, might in fact be similar to the bulk modes of high defect densities predicted by the operator method, but this supposition will require future investigation.

In addition to defect densities, I plan to study the effects of dislocations on material lattices. In Section 3.3 it was shown that parameters p and q could be used to approximate the spectrum of a fully relaxed lattice with a single vacancy. Next I would like to determine if similar parameters could be utilized along dislocation planes to emulate the spectrum of a substance with dislocations. It would also be interesting to compare the spectral shifts induced by dislocations to the spectral shifts induced by point defects. I expect there to be clear differences in the spectra of the two defect types.

While the operator methodology was fully derived within this work, the number of potential applications to explore in the future are numerous.

Appendix A: Orthogonality Conditions

In this section, I examine the situations in which the orthogonality condition (2.6) is met. I classify the lattice types of interest by the nodal connectivity, Z_k , which is the total number of interactions involving the k th node in the reference unit cell. In general, I have found that the orthogonality condition is satisfied when the nodal connectivity satisfies

$$Z_k \leq 2n, \forall k \tag{A.1}$$

where n is the number of spatial dimensions. Note that this is independent of the lattice symmetry and generally precludes lattices with bases. As an example, I will first consider the primitive triclinic unit cell shown in Fig. A.1a. The triclinic lattice has the lowest symmetry, and other lattice types such as cubic, orthorhombic, monoclinic, etc. may be considered special cases of the triclinic lattice. I restrict the present consideration to only triclinic lattices where the angles and cell dimensions are such that the nearest neighbor interactions occur along the lines drawn from the lattice vectors. Very elongated cells or cells with very low or high aspect ratios are beyond the present scope. The simple, triclinic lattice has a nodal connectivity of $Z_k = 6 \forall k$.

By definition, primitive unit cells contain a single node, and thus $k = 1$ and

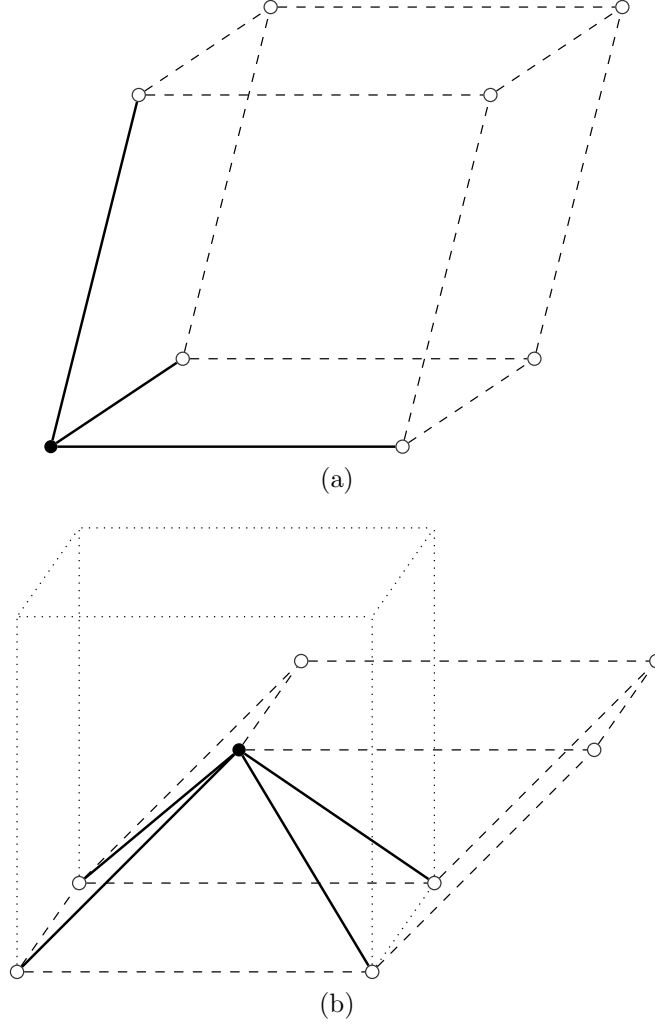


Figure A.1: (a) Triclinic primitive cell with the three independent interactions denoted by the solid lines. (b) The body-centered cubic unit cell (dotted lines) with the primitive cell shown with dashed lines. The four independent nearest-neighbor interactions are represented by solid lines.

$k' = 1$ for every interaction. I will therefore omit the subscript 11 for simplicity. The pristine dynamical matrix for any primitive unit cell comes from using Eq. (2.31) in (2.27) to yield

$$\mathbf{D}_p = \sum_{\nu'} c_{\nu'} \mathbf{v}_{\nu'} \quad (\text{A.2})$$

where $c_{\nu'} = 2\phi_{\nu'} (1 - \cos(\mathbf{G} \cdot \mathbf{r}^{0\nu'}))$. The primitive cell of a triclinic lattice, as de-

picted in Fig. [A.1a](#) has exactly three interactions per cell, and thus

$$\mathbf{D}_p = c_1 \mathbf{v}_1 + c_2 \mathbf{v}_2 + c_3 \mathbf{v}_3 \quad (\text{A.3})$$

To calculate the orthogonality condition, the general form of Δ must be found for a primitive lattice. Using Eqs. [\(2.21\)](#) and [\(2.42\)](#) in [\(2.9\)](#),

$$\Delta_{l'} = (1 - q_{l'}) c_{l'} \hat{\mathbf{n}}_{l'} \hat{\mathbf{n}}_{l'}^T \quad (\text{A.4})$$

Consider now Δ_m and Δ_n such that the orthogonality condition [\(2.6\)](#) becomes

$$\Delta_m \mathbf{D}_p^{-1} \Delta_n = (1 - q_m)(1 - q_n) c_m c_n \hat{\mathbf{n}}_m \hat{\mathbf{n}}_m^T \mathbf{D}_p^{-1} \hat{\mathbf{n}}_n \hat{\mathbf{n}}_n^T \quad (\text{A.5})$$

In the above expression, the scalar terms are non-zero in general and, therefore, condition [\(2.6\)](#) is met if

$$\hat{\mathbf{n}}_m^T \mathbf{D}_p^{-1} \hat{\mathbf{n}}_n = 0 \quad (\text{A.6})$$

where

$$\hat{\mathbf{n}}_{l'} = \begin{pmatrix} n_{l'1} \\ n_{l'2} \\ n_{l'3} \end{pmatrix} \quad (\text{A.7})$$

Let us now examine the conditions under which [\(A.6\)](#) is true. Substituting [\(A.3\)](#) and [\(A.7\)](#) into [\(A.6\)](#), we find that the left-hand-side of [\(A.6\)](#) for $m = 1$ and $n = 2$

becomes

$$\hat{\mathbf{n}}_1^T \mathbf{D}_p^{-1} \hat{\mathbf{n}}_2 = \frac{c_2 c_3 \det([\hat{\mathbf{n}}_1, \hat{\mathbf{n}}_2, \hat{\mathbf{n}}_3])}{\det(\mathbf{D}_p)} \begin{pmatrix} n_{22}n_{33} - n_{23}n_{32} \\ n_{23}n_{31} - n_{21}n_{33} \\ n_{21}n_{32} - n_{22}n_{31} \end{pmatrix}^T \begin{pmatrix} n_{21} \\ n_{22} \\ n_{23} \end{pmatrix} \quad (\text{A.8})$$

The last two terms reduce to zero when multiplied. Since no assumptions were made about orientation, the orthogonality condition is satisfied for any primitive lattice with a connectivity of $Z_k = 6$, which agrees with condition (A.1).

Next, consider a primitive lattice with $Z_k = 8$, such as the body-centered-cubic lattice depicted in Fig. A.1b. Note that the body-centered primitive cell in Fig. A.1b has four interactions, and thus the dynamical matrix will be of the form

$$\mathbf{D}_p = c_1 \mathbf{v}_1 + c_2 \mathbf{v}_2 + c_3 \mathbf{v}_3 + c_4 \mathbf{v}_4 \quad (\text{A.9})$$

Now substituting (A.9) into Eq. (A.6), the left-hand side reduces to

$$\hat{\mathbf{n}}_1^T \mathbf{D}_p^{-1} \hat{\mathbf{n}}_2 = \frac{c_3 c_4}{\det(\mathbf{D}_p)} \det([\hat{\mathbf{n}}_1, \hat{\mathbf{n}}_3, \hat{\mathbf{n}}_4]) \det([\hat{\mathbf{n}}_2, \hat{\mathbf{n}}_3, \hat{\mathbf{n}}_4]) \quad (\text{A.10})$$

The orthogonality condition is satisfied when (A.10) reduces to zero. In general, c_3 and c_4 are not zero, and therefore, one of the two determinants must be zero for the orthogonality condition to be satisfied. By definition, three unit vectors are linearly dependent when the matrix composed of the three vectors has a determinant equal to zero. Thus for (A.10) to reduce to zero, $\hat{\mathbf{n}}_1$ and/or $\hat{\mathbf{n}}_2$ must lie on the plane

defined by $\hat{\mathbf{n}}_3$ and $\hat{\mathbf{n}}_4$. However, (A.6) should be satisfied for all $n, m \in (1, 2, 3, 4)$, and so (A.10) must reduce to zero for all permutations of $\hat{\mathbf{n}}_1, \hat{\mathbf{n}}_2, \hat{\mathbf{n}}_3$, and $\hat{\mathbf{n}}_4$. This is only the case when all four vectors lie on one two-dimensional plane, or when two of the unit vectors are parallel. Therefore, the orthogonality condition is not, in general, satisfied for primitive cells with nodal connectivities of $Z_k \geq 8$ in three dimensions. Again, this finding agrees with conditions (A.1).

Bibliography

- [1] Rose Weisburgh and Peter W Chung. *submitted to the International Journal of Solids and Structures*, 2016.
- [2] Zhiqiang Luo, Chunxiao Cong, Jun Zhang, Qihua Xiong, and Ting Yu. The origin of sub-bands in the raman d-band of graphene. *Carbon*, 50(11):4252–4258, 2012.
- [3] Jannik C Meyer, C Kisielowski, R Erni, Marta D Rossell, MF Crommie, and A Zettl. Direct imaging of lattice atoms and topological defects in graphene membranes. *Nano letters*, 8(11):3582–3586, 2008.
- [4] DW Feldman, M Ashkin, and James H Parker Jr. Raman scattering by local modes in germanium-rich silicon-germanium alloys. *Physical Review Letters*, 17(24):1209, 1966.
- [5] S Nakashima, Y Nakatake, Y Ishida, T Talkahashi, and H Okumura. Detection of defects in sic crystalline films by raman scattering. *Physica B: Condensed Matter*, 308:684–686, 2001.
- [6] CM Ruiz, X Fontané, A Fairbrother, V Izquierdo-Roca, C Broussillou, S Bodnar, A Pérez-Rodríguez, and V Bermúdez. Impact of electronic defects on the raman spectra from electrodeposited cu (in, ga) se2 solar cells: Application for non-destructive defect assessment. *Applied Physics Letters*, 102(9):091106, 2013.
- [7] Elliott W Montroll and Renfrey B Potts. Effect of defects on lattice vibrations. *Physical Review*, 100(2):525, 1955.
- [8] AA Maradudin. Some effects of point defects on the vibrations of crystal lattices. *Reports on Progress in Physics*, 28(1):331, 1965.
- [9] IM Lifshitz and AM Kosevich. The dynamics of a crystal lattice with defects. *Reports on Progress in Physics*, 29(1):217, 1966.

- [10] Sulin Zhang, Steven L Mielke, Roopam Khare, Diego Troya, Rodney S Ruoff, George C Schatz, and Ted Belytschko. Mechanics of defects in carbon nanotubes: atomistic and multiscale simulations. *Physical Review B*, 71(11):115403, 2005.
- [11] Mahmoud I Hussein, Michael J Leamy, and Massimo Ruzzene. Dynamics of phononic materials and structures: Historical origins, recent progress, and future outlook. *Applied Mechanics Reviews*, 66(4):040802, 2014.
- [12] MM Sigalas. Defect states of acoustic waves in a two-dimensional lattice of solid cylinders. *Journal of Applied Physics*, 84(6):3026–3030, 1998.
- [13] E Peter Carden and Paul Fanning. Vibration based condition monitoring: a review. *Structural health monitoring*, 3(4):355–377, 2004.
- [14] DJ Colquitt, IS Jones, NV Movchan, and AB Movchan. Dispersion and localization of elastic waves in materials with microstructure. In *Proceedings of the Royal Society of London A: Mathematical, Physical and Engineering Sciences*, volume 467, pages 2874–2895. The Royal Society, 2011.
- [15] Alvar M Kabe. Stiffness matrix adjustment using mode data. *AIAA journal*, 23(9):1431–1436, 1985.
- [16] M Lifšic. Some problems of the dynamic theory of non-ideal crystal lattices. *Il Nuovo Cimento (1955-1965)*, 3:716–734, 1956.
- [17] Markus Grimm and Max Wagner. Mode densities of defect lines in three-dimensional montroll-potts lattices. *Physica A: Statistical Mechanics and its Applications*, 210(1):1–23, 1994.
- [18] Hengji Zhang, Geunsik Lee, and Kyeongjae Cho. Thermal transport in graphene and effects of vacancy defects. *Physical Review B*, 84(11):115460, 2011.
- [19] RG Hutchinson and NA Fleck. The structural performance of the periodic truss. *Journal of the Mechanics and Physics of Solids*, 54(4):756–782, 2006.
- [20] LI Slepyan. Crack in a material-bond lattice. *Journal of the Mechanics and Physics of Solids*, 53(6):1295–1313, 2005.
- [21] E Nolde, RV Craster, and J Kaplunov. High frequency homogenization for structural mechanics. *Journal of the Mechanics and Physics of Solids*, 59(3):651–671, 2011.
- [22] G Theocharis, M Kavousanakis, PG Kevrekidis, Chiara Daraio, Mason A Porter, and IG Kevrekidis. Localized breathing modes in granular crystals with defects. *Physical Review E*, 80(6):066601, 2009.

- [23] Neil Boechler, Georgios Theocharis, and C Daraio. Bifurcation-based acoustic switching and rectification. *Nature materials*, 10(9):665–668, 2011.
- [24] N Boechler, J Yang, G Theocharis, PG Kevrekidis, and C Daraio. Tunable vibrational band gaps in one-dimensional diatomic granular crystals with three-particle unit cells. *Journal of Applied Physics*, 109(7):074906, 2011.
- [25] Scott W Doebling, Charles R Farrar, Michael B Prime, and Daniel W Shevitz. Damage identification and health monitoring of structural and mechanical systems from changes in their vibration characteristics: a literature review. Technical report, Los Alamos National Lab., NM (United States), 1996.
- [26] Peter C Chang, Alison Flatau, and SC Liu. Review paper: health monitoring of civil infrastructure. *Structural health monitoring*, 2(3):257–267, 2003.
- [27] Richard G Cobb and Brad S Liebst. Structural damage identification using assigned partial eigenstructure. *AIAA journal*, 35(1):152–158, 1997.
- [28] Felix Bloch. Über die quantenmechanik der elektronen in kristallgittern. *Zeitschrift für physik*, 52(7-8):555–600, 1929.
- [29] Charles Kittel. *Introduction to solid state physics*. Wiley, 2005.
- [30] Murray S Daw and M Io Baskes. Semiempirical, quantum mechanical calculation of hydrogen embrittlement in metals. *Physical review letters*, 50(17):1285, 1983.
- [31] Murray S Daw and Michael I Baskes. Embedded-atom method: Derivation and application to impurities, surfaces, and other defects in metals. *Physical Review B*, 29(12):6443, 1984.
- [32] SM Foiles, MI Baskes, and Murray S Daw. Embedded-atom-method functions for the fcc metals cu, ag, au, ni, pd, pt, and their alloys. *Physical Review B*, 33(12):7983, 1986.
- [33] RA Johnson. Alloy models with the embedded-atom method. *Physical Review B*, 39(17):12554, 1989.
- [34] DY Sun, MI Mendeleev, CA Becker, K Kudin, Tomorr Haxhimali, M Asta, JJ Hoyt, A Karma, and DJ Srolovitz. Crystal-melt interfacial free energies in hcp metals: A molecular dynamics study of mg. *Physical Review B*, 73(2):024116, 2006.
- [35] Julian D Gale. Gulp: A computer program for the symmetry-adapted simulation of solids. *Journal of the Chemical Society, Faraday Transactions*, 93(4):629–637, 1997.
- [36] Tomas Baer and William L Hase. *Unimolecular reaction dynamics: theory and experiments*. Number 31. Oxford University Press on Demand, 1996.

- [37] Conyers Herring. Role of low-energy phonons in thermal conduction. *Physical Review*, 95(4):954, 1954.
- [38] George AF Seber and Alan J Lee. *Linear regression analysis*, volume 936. John Wiley & Sons, 2012.
- [39] Stuart Rosen and Peter Howell. *Signals and systems for speech and hearing*, volume 29. Brill, 2011.
- [40] N Boechler, G Theocharis, Stéphane Job, PG Kevrekidis, Mason A Porter, and C Daraio. Discrete breathers in one-dimensional diatomic granular crystals. *Physical review letters*, 104(24):244302, 2010.